

1 Observations and hypotheses related to low to middle free tropospheric aerosol, water vapor and
2 altocumulus cloud layers within convective weather regimes: A SEAC⁴RS case study

3 Jeffrey S. Reid^{1*}, Derek J. Posselt², Kathleen Kaku³, Robert A. Holz⁴, Gao Chen⁵, Edwin W.
4 Eloranta⁴, Ralph E. Kuehn⁴, Sarah Woods⁶, Jianglong Zhang⁷, Bruce Anderson⁵, T. Paul Bui⁸,
5 Glenn S. Diskin⁵, Patrick Minnis^{5#}, Michael J. Newchurch⁹, Simone Tanelli², Charles R. Trepte⁵,
6 K. Lee Thornhill⁵, Luke D. Ziemba⁵

7 ¹US Naval Research Laboratory, Marine Meteorology Division Monterey CA

8 ²Jet Propulsion Laboratory, Pasadena CA

9 ³General Dynamics Information Technology, Naval Research Laboratory, Monterey CA

10 ⁴Space Sciences Engineering Center, University of Wisconsin, Madison WI

11 ⁵NASA Langley Research Center, Science Directorate, Hampton VA

12 ⁶SPEC Inc. Boulder CO.

13 ⁷University of North Dakota, Grand Forks, ND

14 ⁸NASA Ames Research Center, Mountain View, CA

15 ⁹Atmospheric Science Department, University of Alabama in Huntsville, Huntsville, AL

16 [#]Now at Science Systems and Applications, Hampton, VA

17

18 Key points:

19 1) Highly sensitive lidar and aircraft observations reveal thin aerosol detrainment layers
20 from convection and their associated altocumulus clouds.

21 2) At 0°C there is a proclivity for aerosol and water vapor detrainment from storms, in
22 association with melting level Altocumulus shelves.

23 3) Detraining particles undergo chemical and microphysical transformations with enhanced
24 nucleation in cleaner environments.

25

26

27 *Corresponding author: Jeffrey S. Reid (jeffrey.reid@nrlmry.navy.mil)

28

29 **Abstract:** The NASA *Studies of Emissions & Atmospheric Composition, Clouds & Climate*
30 *Coupling by Regional Surveys* (SEAC⁴RS) project included goals related to aerosol particle
31 lifecycle in convective regimes. Using the University of Wisconsin High Spectral Resolution
32 Lidar system at Huntsville, Alabama USA and the NASA DC-8 research aircraft, we investigate
33 the altitude dependence of aerosol, water vapor and Altocumulus (Ac) properties in the free
34 troposphere from a canonical August 12, 2013 convective storm case as a segue to a presentation
35 of a mission wide analysis. It stands to reason that any moisture detrainment from convection
36 must have an associated aerosol layer. Modes of covariability between aerosol, water vapor and
37 Ac are examined relative to the boundary layer entrainment zone, 0°C level, and anvil, a region
38 known to contain Ac clouds and a complex aerosol layering structure (Reid et al., 2017).
39 Multiple aerosol layers in regions warmer than 0°C were observed within the PBL entrainment
40 zone. At 0°C there is a proclivity for aerosol and water vapor detrainment from storms, in
41 association with melting level Ac shelves. Finally, at temperatures colder than 0°C, weak aerosol
42 layers were identified above Cumulus congestus tops (~0°C and ~-20°C). Stronger aerosol
43 signals return in association with anvil outflow. In situ data suggest that detraining particles
44 undergo aqueous phase or heterogeneous chemical or microphysical transformations, while at the
45 same time larger particles are being scavenged at higher altitudes leading to enhanced nucleation.
46 We conclude by discussing hypotheses regarding links to aerosol emissions and potential indirect
47 effects on Ac clouds.

48 **Plain language summary:** In studies of the vertical transport of air pollution by clouds as well
49 as pollution's subsequent impact on those clouds the scientific community often focuses on
50 clouds with bases at the planetary boundary layer (such as typical fair weather cumulus) and the
51 outflow from thunderstorms at their tops. However, new highly sensitive lidar systems
52 demonstrate complex aerosol features in the middle free troposphere. Aerosol layers formed in
53 convective outflow are explored and are shown to have strong relationships to mid-level
54 tropospheric clouds, an important but difficult-to-model or monitor cloud regime for climate
55 studies.

56
57

58 **1.0 Introduction**

59 Much of the focus of aerosol-cloud radiation studies (i.e., the first indirect effect) has been on
60 either Planetary Boundary Layer (PBL) Stratocumulus (Sc) or Cumulus clouds (Cu, e.g.,
61 Twomey et al., 1977 and many subsequent citations), or the injection of aerosol particles and
62 their precursors into the upper troposphere/lower stratosphere by deep precipitating convection
63 from Cumulonimbus (Cb, e.g., Pueschel et al., 1997; Kulmala et al., 2004; Waddicor et al., 2012;
64 Saleeby et al., 2016), pyro-convection (e.g., Fromm et al., 2008; 2010; Lindsay and Fromm
65 2008) and volcanic activity (e.g., Jensen and Toon 1992; DeMott et al., 1997; Amman et al.,
66 2003). However, there is a third important but often overlooked aerosol-cloud system related to
67 mid-level clouds. Altostratus (Ac) clouds in the lower to middle free troposphere (LMFT) are
68 generated by numerous mechanisms (e.g., synoptic forcing, gravity waves, orographic waves),
69 but are particularly prevalent in convective regimes (Heymsfield et al., 1993; Parungo et al.,
70 1994; Sassen and Wang, 2012). Indeed, the above authors and others (e.g., Gedzelman, 1988)
71 note these cloud types receive comparatively little attention in the scientific community relative
72 to their importance. Forecasters sometimes ignominiously note the presence of Ac in convective
73 environments as “midlevel convective debris.” Yet, Cloud-Aerosol-Lidar with Orthogonal
74 Polarization (CALIOP) and CloudSat retrievals attribute to Ac as much as 30% area coverage in
75 Southeast Asia and the summertime eastern continental United States (e.g., Zhang et al., 2010;
76 Sassen and Wang, 2012; Zhang et al., 2014). This is in agreement with observer-based cloud
77 climatologies (e.g., Warren et al., 1986; 1988).

78 A long-standing hypothesis by Parungo et al., (1994) suggested that globally increasing aerosol
79 emissions would lead to higher mid troposphere aerosol loadings, in turn enhancing Ac
80 reflectance and perhaps Ac lifetime. This is plausible, as Kaufman and Fraser (1997) who
81 observed strong relationships between aerosol loading and cloud effective radius over the
82 Amazon, likely mistook Sc and Ac clouds for Cumulus mediocris (Cu) in their analysis of cloud
83 reflectivity and lifetime impacts by biomass burning particles (Reid, 1998; Reid et al., 1999).
84 Lidar studies by Schmidt et al., (2015) showed significant sensitivity of cloud droplet size
85 distributions to aerosol particles near cloud base. Yet Ac’s diurnal cycle, covariance with other
86 cloud types including cirrus during convective detrainment, and sometimes tenuous cloud optical
87 depth make Ac clouds difficult to characterize and monitor. In an inter-comparison study for
88 Southeast Asia, Reid et al., (2013) found more diversity in midlevel cloud fractions between

89 satellite products than at any other level. Likewise, large scale models tend to underestimate Ac
90 formation and liquid water content (Barrett et al., 2017).

91 Ac clouds are prevalent in many forms such as: castellanus, an indicator of midlevel instability;
92 mountain wave lenticularis; and translucidus (or colloquially mackerel sky). One class of Ac
93 clouds, colloquially referred to as shelf clouds, is caused in part by detrainment at mid-level from
94 deep convection (Fig. 1(a); see Johnson et al., 1999; Yasunga et al., 2006). These clouds are not
95 assigned their own genus in the International Cloud Atlas (Cohen et al., 2017), but the generic Ac
96 is recognized as associated with the spreading of convective elements at a stable layer.

97 We know that Ac cloud prevalence is strongly associated with convective environments, such as
98 in association with the Madden Julian Oscillation (Riley et al., 2011). Ac shelves often form at
99 0°C from deep convection or in association with mid-level inversions (e.g., Johnson et al., 1996,
100 1999; Riihimaki et al., 2012). A primary production mechanism is thought to be related to the
101 formation of 0°C stable layers initiated by the melting of falling frozen hydrometeors and
102 enhanced condensation to compensate for the cooling (Posselt et al., 2008; Yasunga et al., 2008).
103 Hydrometeor evaporation processes discussed in Posselt et al (2008) have likewise been
104 hypothesized to help form the inversion. This results in a thin cloud feature forming just below
105 the inversion. Shelf-like Ac from towering cumulus (TCu) are also frequently observed (Fig.
106 1(b)), and may be related to the detrainment of overshooting tops around regional 0°C stable
107 layers formed by surrounding convection (Johnson et al., 1996), or upper level subsidence.
108 Combined Ac and associated Alto stratus (As) coverage can be high in convectively active
109 regions (Fig. 1(c)). Ac can also form overnight from the residual PBL and then burn off during
110 the day (Fig. 1(d); Reid et al., 2017; Wood et al., 2018) or during fair weather conditions just
111 ahead of more active weather (Fig. 1(e)). Ac formation by mesoscale lifting is also common.
112 Although sometimes geometrically thin with low liquid water contents, Ac can generate copious
113 virga (Fig. 1(f)).

114 Compared to other cloud species, the relationship between LMFT aerosol layers and Ac clouds
115 has a small literature base. The largest fraction of papers relate to lidar observations of smoke
116 and dust as ice nuclei (IN) in mixed-phased alto clouds (e.g., Hogan et al., 2003; Sassen et al.,
117 2003; Wang et al., 2004; Sassen and Khvorostyanov, 2008; Ansmann et al., 2009; Wang et al.,
118 2015). However, cloud condensation nuclei (CCN) budgets for these cloud types have not been

119 studied in detail with in situ observations, particularly for entirely liquid clouds. The complex
120 mixed-phase nature of alto-level clouds and stratiform precipitation coupled with their thin
121 nature and low updraft velocities (Schmidt et al., 2014) likely lead to sensitivity to even small
122 perturbation in CCN concentration (Reid et al., 1999; Schmidt et al., 2015; Wang et al., 2015).
123 Clouds can serve as aqueous phase reactors of gas and aerosol particle species, even hosting
124 nucleation events (Hegg et al., 1991), while evaporating droplets and precipitation leave residual
125 aerosol particles. Given that Ac clouds are observed to have a strong impact in shortwave solar
126 radiation (Sassen and Khvorostyanov, 2007), the hypotheses of Parungo et al., (1994) are worthy
127 of consideration despite initial skepticism (e.g., Norris 1999). Only now are the tools becoming
128 available to quantitatively investigate further.

129 Observing the aerosol-Ac environment is challenging. The scarcity of data for alto-level aerosol
130 layers in the convective regimes where Ac clouds often form, combined with the contextual or
131 sampling biases inherent for the in situ observations of such layers and sun-synchronous polar-
132 orbiting aerosol observations, obscure the true importance of LMFT aerosol layers in
133 atmospheric aerosol lifecycle and Ac cloud physics. An opportunity for study arose with the
134 summer 2013 NASA *Studies of Emissions & Atmospheric Composition, Clouds & Climate*
135 *Coupling by Regional Surveys* (SEAC⁴RS; Toon et al., 2016) field mission. For SEAC⁴RS, the
136 NASA DC-8, NASA ER-2 and Spec Inc Lear-25 aircraft were deployed along with ground assets
137 including the University of Wisconsin Space Science and Engineering Center (SSEC) High
138 Spectral Resolution Lidar (UW-HSRL) to examine the aerosol and cloud environment of the
139 summertime eastern United States (Toon et al., 2017; Reid et al., 2017). These observations
140 allowed for comprehensive measurements of the structure and microphysical properties of local
141 convectively generated LMFT aerosol layers.

142 SEAC⁴RS provided a valuable but complex dataset-especially in the vicinity of active
143 convection. To simplify the analysis, this paper provides a case study of the covariability
144 between aerosol layers and LMFT Ac clouds in convective environments using observations
145 collected on August 12, 2013 (Fig. A.1). This day was chosen due to the isolated regional nature
146 of the convection that occurred, and availability of ground based lidar and airborne DC-8
147 sampling. This analysis will provide context for further exploration of the SEAC⁴RS datasets.

148 For this analysis we define Ac consistent with the WMO definition (Houze 1993; WMO
149 <https://cloudatlas.wmo.int/clouds-definitions.html> last accessed Mar 2018) of mid-altitude (2-7
150 km) clouds that are a) liquid or mixed phase, and b) decoupled from direct surface forcing. We
151 begin with a brief description of data sets used in the remainder of the paper (Section 2). We then
152 provide an overall narrative of the meteorological situation on August 12 (Section 3) followed by
153 an analysis of UW-HSRL (Section 4) and data collected from a nearby storm by the DC-8
154 (Section 5). In the paper’s discussion (Section 6), we explore commonalities in the two datasets,
155 and further explore hypotheses of LMFT layer characteristics, their origins, and relationships to
156 Ac clouds to set the stage for subsequent papers. A final summary and conclusions are presented
157 in Section 7.

158 2.0 Data and Methods

159 The analysis presented here centers around the August 12, 2013 SEAC⁴RS airborne research
160 flight based out of Ellington Field, Houston TX (Toon et al., 2016). The Ellington deployment
161 for the SEAC⁴RS mission was conducted from August 12 -September 23 with three research
162 aircraft (NASA DC-8, NASA ER2, SPEC Learjet 25), an extensive ground network including
163 AERONET sun photometers (Holben et al., 1998; Toon et al., 2016), and the deployment of the
164 UW-HSRL to Huntsville (Reid et al., 2017). Comprehensive descriptions of the field assets are
165 provided in this section’s cited papers; here we provide a short summary of datasets used in this
166 analysis.

167 2.1 UW-HSRL Deployment to Huntsville

168 LMFT aerosol and cloud layers were monitored by a 532 nm UW-HSRL system, deployed by
169 the NASA Cloud-Aerosol Lidar and Infrared Pathfinder Satellite Observations (CALIPSO)
170 science team to enhance monitoring at the Regional Atmospheric Profiling Center for Discovery
171 (RAPCD) lidar facility at the UAH National Space Sciences Technology Center (NSSTC)
172 building (-34.725 ° N; 86.645° W), from June 18 to November 4, 2013. The RAPCD facility is
173 located on the western side of the city of Huntsville at an elevation of ~220 m. Including
174 building height, the lidar transmitter was situated at 230 m above mean sea level (MSL). Overall
175 the local terrain is flat, with the exception of a line of hills protruding an additional 200-350 m
176 and located 10-15 km to the east and southeast. The UW-HSRL was hardened for continuous
177 use, and collected contiguous aerosol backscatter and depolarization data every 1 minute at 30 m
178 vertical resolution. The only significant notable outages were from August 20-22 and September

179 13-17. UW HSRL observations can be visualized and downloaded through the SSEC HSRL web
180 page (<http://hsrl.ssec.wisc.edu/>), last verified in February 2019).

181 The UW-HSRL was able to extract the aerosol backscatter profile to very high fidelity. Unlike
182 more common elastic backscatter lidar measurements that must de-convolve a combined
183 molecular and aerosol signal in an inversion, HSRL systems can separate a line broadened
184 molecular backscatter signal from the total backscatter signal via a notch filter (Eloranta et al.,
185 2005, 2014; Hair et al., 2008). The difference is used to calculate aerosol backscatter. For this
186 deployment the UW HSRL performed with a precision in aerosol backscatter of better than 10^{-7}
187 $(\text{m sr})^{-1}$ for a 1 minute average, and $10^{-8} (\text{m sr})^{-1}$ for 15 minute averages. In comparison, Rayleigh
188 backscattering is $1 \times 10^{-6} (\text{m sr})^{-1}$ at 4 km, and $5 \times 10^{-7} (\text{m sr})^{-1}$ at 10 km. Thus at 15 min averaging,
189 precision is likewise better than 1 to 5% of Rayleigh. This very high sensitivity to aerosol
190 scattering is a result of the combination of the aforementioned HSRL ability to separate the
191 molecular from aerosol scattering, the large signal to noise of the instrument, and the high solar
192 background rejection during daytime observations. It is challenging to make a direct comparison
193 of the ground based HSRL to CALIOP given the very different viewing and sampling combined
194 with the highly variable SNR of CALIOP between day/night observations. The NASA Langley
195 airborne HSRL was used to validate the CALIPSO aerosol retrievals (S.P Burton et al. 2013) and
196 found that only 13% of the layers identified as smoke by the Langley HSRL was correctly
197 identified by CALIOP using the V3 CALIOP products. The UW HSRL, being a stationary
198 ground-based system, provides even greater sensitivity to the aerosol backscatter as it can dwell
199 over the same location for a long period of time.

200 By calculating the slope of the returned molecular scattering, aerosol light extinction can be
201 directly calculated. However, as described in Reid et al., (2017), there are several caveats. First,
202 there must be significant enough signal to calculate the slope; in this instrument, extinction must
203 be greater than 0.1 km^{-1} . Second, one must account for an “overlap correction” in the near field,
204 accounting for the fact that the telescope is not fully in focus until a range of about 4.5 km from
205 the system. The signal below the 4.5 km level appeared to vary in time, sometimes hourly, during
206 the daytime. Consequently, for the altitude range we will study here, it is best to rely on aerosol
207 backscatter. Noting that extinction is simply the aerosol backscatter times the lidar ratio (S_a),

208 here we assume a lidar ratio of 55 sr^{-1} as a baseline (Reid et al., 2017). Expected deviations from
209 this baseline are discussed in the Results and Discussion sections.

210 In addition to the lidar, several other deployments to the UAH site are used here. Most notably,
211 UAH was a Southeast American Consortium for Intensive Ozonesonde Network Study
212 (SEACIONS) release site (<http://croc.gsfc.nasa.gov/seacions/>, last accessed December 17, 2018).
213 Forty sondes were released between August 6 and September 21, 2013, at 18:00-19:00 Z/13:00-
214 14:00 CDT to coincide with early afternoon boundary layer conditions, mid-flight airborne
215 activity, and the NASA A-train overpass. For August 12, 2013, the release time was 13:42 CDT,
216 and is used here for situational awareness and the mapping of cloud and aerosol layers to their
217 temperatures.

218 2.2 The SEAC⁴RS DC-8 Operations

219 The DC-8 conducted 24 flights with patterns that covered the Western United States through the
220 Southeastern United States (SEUS) and into the Gulf of Mexico. Flight patterns often included
221 three primary relevant components. 1) A ~ 100 km curtain wall pattern with multiple flat flight
222 levels from 5 km to the near surface to collect free troposphere, entrainment zone, cloud base and
223 near surface samples; 2) saw toothed transits to monitor the lower troposphere for chemistry
224 applications; and 3) spirals in the vicinity of developing deep convection. Such components are
225 visible in this day's flight (Fig. A.1). Flight restrictions in the vicinity of Huntsville prevented
226 vertical profiles directly over the UW-HSRL. Nevertheless, the DC-8 had ample opportunity to
227 sample the SEUS LMFT environment, in particular for the case of August 12, 2013 examined
228 here.

229 The DC-8 hosted its most comprehensive instrument suite ever to support the chemistry,
230 convection, radiation, and upper troposphere/lower stratosphere (UTLS) science goals and
231 customers. However, for the particular test case and application examined here, there are several
232 caveats worth noting. While the ground-based UW HSRL can detect the fine aerosol structure in
233 convective environments and in the vicinity of Ac clouds, generating in situ observations to
234 correspond to this structure is difficult. At flight speeds of $\sim 120\text{-}150 \text{ m s}^{-1}$, the DC-8 is only in a
235 detrainment patch for a few seconds, causing difficulty in differentiating small-scale aerosol
236 features. Further, the massive payload of the DC-8, although comprehensive, also leads to
237 functional problems as instrument calibration, maintenance, and scanning cycles were not

238 synchronized. Shattering effects of liquid cloud droplets and ice further disrupted the sampling of
239 the very near cloud environment. Thus, one cannot retrieve full complement of all data for an
240 entire profile or flight component, let alone for individual features that the DC-8 might observe
241 for less than 10 seconds. While the DC-8 carried a lidar system of its own, stand-off distances
242 from the aperture and cloud heterogeneity prevented its use in this particular analysis.
243 Nevertheless, the DC-8 hosted a number of instruments that can provide a valuable view of the
244 overall aerosol and cloud structure in the August 12 2013 convective environment which can be
245 coupled with the lidar observations. These key instruments are listed here:

246 1) State variables: Navigation was derived from DC-8 housekeeping variables. Pressure,
247 temperature and winds were measured by the NASA Ames Meteorological Measurement System
248 (MMS, Scott et al., 1990). Moisture related variables were derived from the NASA Langley
249 Diode Laser Hygrometer (DLH, Podolske et al., 2003; Livingston et al., 2008).

250

251 2) Aerosol physical and optical properties: Baseline aerosol number, size, and optical
252 properties were derived from the Langley Aerosol Research Group Experiment
253 (<https://airbornescience.nasa.gov/instrument/LARGE>, Ziemba et al., 2013; Corr et al., 2016)
254 instrument set, which included continuously sampling nephelometer, CN, and optical particle
255 encounters. The LARGE package monitored aerosol particles from ultrafine CN to an inlet cut
256 point of $\sim 3.5 \mu\text{m}$, and units reflect volumetric scaling to a standard temperature and pressure of
257 20°C and 1013 hPa. To prevent any possible cloud water or precipitation shattering effects on the
258 aerosol instruments, CN, nephelometer, and LAS data were heavily cloud screened with data
259 points removed for one second before the arrival and two seconds after the exit of any cloud with
260 $\text{LWC} > 0.005 \text{ g m}^{-3}$.

261 3) Aerosol chemistry: Aerosol chemistry was evaluated using data from the CU aircraft HR-
262 AMS (Canagaratna et al., 2007; Dunlea et al., 2009; [http://cires1.colorado.edu/jimenez-](http://cires1.colorado.edu/jimenez-group/wiki/index.php/FAQ_for_AMS_Data_Users)
263 [group/wiki/index.php/FAQ_for_AMS_Data_Users](http://cires1.colorado.edu/jimenez-group/wiki/index.php/FAQ_for_AMS_Data_Users) last accessed Mar 2018) that reports the
264 composition of submicron non-refractory particles. Reported O/C and OA/OC ratios from this
265 instrument were derived using the updated calibration of Canagaratna et al (2015). Unlike single
266 particle instruments, the AMS is fairly insensitive to inlet artifacts during cloud penetration. Data

267 points that were flagged as being potentially impacted by such artifacts (by monitoring excess
268 water and/or zinc in the aerosol mass spectrum) were removed prior to analysis.

269 4) Cloud properties: Cloud detection properties were derived from the SPEC microphysics
270 package (e.g., Lawson 2011; Lawson et al., 2001; 2006; 2010), in particular the Fast Cloud
271 Droplet Probe (FCDP) which provided the core cloud liquid water product and the 2D-2 for ice
272 identification.

273 5) Gas chemistry: While the DC-8 carried comprehensive gas chemistry instrumentation, for
274 this overview case study we rely on CO from the Differential Absorption CO measurement
275 (DACOM, Sachse et al., 1987; McMillan et al., 2011), CO₂ from Non-dispersive IR Analyzer
276 measurements (Vay et al., 2011) and SO₂ from mass spectroscopy (Kim et al., 2007),.

277 2.3 Ancillary datasets:

278 In the analysis presented here multiple data sets were examined, but for brevity are not shown in
279 detail here. Regional meteorology was diagnosed through a combination of NEXRAD radar
280 (NOAA NWS, 1991), GOES-13 geostationary and MODIS satellite datasets and models.
281 Baseline meteorology was provided by a Coupled Ocean Atmosphere Mesoscale Prediction
282 System (COAMPS[®]) analysis including NEXRAD precipitation and wind assimilation (Zhao et
283 al., 2008; Lu et al., 2011). Operational MODIS aerosol (MOD/MYD04, Levy et al., 2013) and
284 cloud (MOD/MYD 06, Platnick et al., 2003; 2016) were also used. Geostationary imagery was
285 generated at Space Sciences and engineering center with cloud products generated by Minnis et
286 al. (2008). Regional aerosol concentrations were taken from South Eastern Aerosol Research and
287 Characterization (SEARCH, Edgerton et al., 2015) and Chemical Speciation Network (CSN),
288 and Aerosol Robotic Network (AERONET, Holben et al., 1998) sun photometer data. Back
289 trajectories were utilized from HYSPLIT (Stein et al., 2015).

290 **3.0 Regional context for the August 12th case**

291 Analysis of the August 12, 2013 case study is greatly aided by context provided by a regional
292 weather analysis guided by satellite and lidar observations. A more detailed meteorological
293 analysis is provided in Supplemental Appendix A. In short, on August 12, 2103 the SEUS was in
294 a fair weather summertime convective regime, with copious small convective, congestus and
295 isolated Cbs. Images of the cloud field from MODIS and on-aircraft photography are provided in
296 Fig. 2 (including MOD/MYD cloud top temperatures). Corresponding afternoon radiosonde

297 sounding at UAH are also provided in Fig. 3 (release 18:40 GMT; 13:40 local CDT time) with
298 (a) temperature and dewpoint; (b) water vapor mixing ratio; and (c) wind speed and direction.
299 The diurnal pattern of convection is also provided in NEXRAD composite radar images taken
300 throughout the day, which are provided in Appendix Fig. A.2.

301 By daybreak on August 12, the convection of the previous day had largely subsided over
302 Alabama (Figs. A.2 (b) and (c)). Northern Alabama experienced developing Cu and Ac, with
303 cirrus (Ci) intermixed to the north in the morning hours (e.g., Terra MODIS 16:00 UTC, Figs.
304 2(a) and (c)) in association with the stationary front. Continuing southward, cloud fractions
305 outside of the cirrus and Ac domain ranged from 70-90%. Just before the Terra overpass, isolated
306 convection was initiated throughout the region, including several cells north and east of the UAH
307 site. By early afternoon (Aqua MODIS 19:14 UTC, Figs. 2(b) and A.2 (d) and (e)), isolated
308 precipitating cells were widespread across the region. At the same time, cloud fractions
309 diminished significantly, with a notable reduction in mid-level Ac (yellow to light green colors).
310 Low level cloud fractions diminished up to ~60%, but there were larger numbers of isolated and
311 higher-topped TCu.

312 Of note here is the large area of optically thin $\sim 0^{\circ}\text{C}$ clouds, presumably melting level Ac,
313 extended southward from the more convectively active regions to the northwest at Terra
314 overpass. MODIS cloud retrievals suggest the associated Ac clouds were in the 3 to -3°C range,
315 with effective radius values on the order of 8-10 μm and liquid water paths of $\sim 10\text{-}30\text{ g m}^{-3}$.
316 However inspection of the RGB images shows these clouds as semitransparent and it is unclear
317 as to what the retrievals are sensitive to. The implications of this observation are elaborated on
318 further in the discussion section.

319 Using the DC-8 forward-looking cameras during its flight on August 12, $\sim 21:16$ UTC allows us
320 to categorize the cloud types and heights of the cloud bases and cloud tops of the observed
321 clouds at the time of the flight (Fig 2e-h). Forward camera images of the environment very near
322 the deepest convection are provided in Fig. 2(f), and (g), respectively, with a final nadir image of
323 the Ac field departing the Cb in Fig 2(h). TCu and Cbs were more isolated, relative to the Ac,
324 forming in association with the remnant outflow boundaries from previous storms, rather than in
325 organized and sustained lines. Clearly visible in Fig 2(e) is a cloud base delineating the mixed
326 layer and the PBL entrainment zone at ~ 1.5 km, corresponding well to the UAH sounding. This

327 entrainment zone was populated by Cumulus humilis (CuHu) to Cu with tops based on the DC-8
328 DIAL HSRL in the 1.5-3.8 km AGL range, functionally defining the top of the PBL. Larger Cu
329 occasionally rose to as high as 4.5-5 km, or to roughly the 0°C level (or ~ 5 km from the
330 sounding, but as shown later as low as 4.6 km from the DC-8). TCu rose to 6-6.5 km, with
331 isolated Cb tops at 12 km. Between the PBL top and the Cb anvils, layers of Ac clouds were
332 prevalent. Some of these Ac clouds are related to mid-level detrainment from Cbs, others are
333 clearly emanating near the tops of TCu (e.g., Fig 2(f)-(h)). Near surface haze was also visible,
334 with Aqua MODIS and AERONET reporting 550 nm AOD on the order of 0.25-0.35. Reported
335 PM_{2.5} was on the order of ~8 μg m⁻³.

336 At the time of the early afternoon UAH radiosonde release, the sounding was typical for the area
337 for a moderately unstable convective meteorological regime (Fig. 3), with the mixed layer and
338 top inversion at 1500 m MSL (1280 AGL; Fig. 3(a)). Water vapor mixing ratio (Fig. 3(b)) was
339 constant, as expected in the mixed layer, falling off rapidly with altitude above, and with small
340 perturbations associated with temperature inversions. Winds were near constant at 250° above
341 the mixed layer, and with steady increases to 12 m s⁻¹ at the 0°C melting level at 4.6 km
342 providing only a modest amount of shear (Fig 3(c)). Derived CAPE from the UAH sounding was
343 1650 J kg⁻¹ (moderate instability) consistent with TCu to isolated Cb development. As discussed
344 in the next section, the corresponding HSRL aerosol backscatter profiles for this release are in
345 Fig 3(d)).

346 4.0 Results I: HSRL observations

347 While the above analysis qualitatively describes the nature of the cloud fields, the time series of
348 aerosol backscatter and depolarization from the UW-HSRL from August 12, 0:00 UTC through
349 Aug 13, 09:00 UTC (Fig. 4 (a) and (b), respectively) provides a quantitative representation of the
350 intricate regional aerosol and cloud environment. Lidar data in Fig. 4 was averaged over 1
351 minute intervals and over 30 m vertical layers, and represents a time period that extended from
352 local sunset of August 11 through daybreak on August 13. Included for reference are ceilometer-
353 like cloud bases identified in the lidar data for liquid and ice clouds (Fig 4(c)), with associated
354 geostationary derived cloud tops. Recall, key temperature, water vapor and wind levels included
355 from the August 12, 18:40 UTC SEACIONS radiosonde release are further provided in Fig. 3(a),
356 (b) and (c) respectively and HSRL aerosol backscatter profiles within +/- 3-hours in (d).

357 Temperature levels from this release are included in Fig. 4. Likewise, mean and individual
358 aerosol backscatter profiles (every other 5 minutes average, 30 m resolution) are included in Fig.
359 3(d) for the two hours after the sounding when the DC-8 was sampling northern Alabama.

360 The meteorology and aerosol profiles depicted in Fig. 4 show considerable fine scale structure in
361 cloud and aerosol features. Considered in concert with Fig. 3, Fig. 4 indicates this day is
362 consistent with the description of the convective environment in Reid et al., (2017) for a similar
363 August 8 2013 case. Thus the description of the overall nature of the aerosol environment does
364 not need to be repeated here in detail, other than to identify the key layers. During the two hour
365 period surrounding the 18:40 UTC radiosonde release, there is: 1) A mixed layer that extends
366 from the surface to 1500 m AGL, identifiable by constant water vapor mixing ratio (ω_v ; Fig. 3b)
367 and an increase in aerosol backscatter in height due to increases in RH with height and hence
368 hygroscopic growth (Fig. 3(d) and 4(a)); 2) Above the mixed layer inversion lies the
369 entrainment zone, including visible detrainment layers; 3) As discussed above and shown in Fig.
370 2(e), the top of the PBL is ambiguous as it relates to cloud tops in a heterogeneous cloud field,
371 but a clear reduction in aerosol backscatter is visible at 4 km, likely related to the tops of regional
372 Cu; 4) A second drop in aerosol backscatter occurs at the 0°C melting level (~4.5 to 5.0 km from
373 regional soundings and the DC-8) on this day; 5) a final aerosol layer between 6-7 km which, as
374 we discuss later, may be associated with cloud top detrainment from TCu. Assuming a baseline
375 $S_a = 55 \text{ sr}^{-1}$ as derived by Reid et al., (2017) an aerosol backscatter of $1 \times 10^{-6} \text{ (m sr)}^{-1}$ (yellow) is
376 equivalent to an aerosol extinction of 0.055 km^{-1} . Integration of aerosol backscatter from the
377 surface to 10 km for cloud free periods with this lidar ratio suggests a 532 nm AOD of ~0.17,
378 dropping to 0.12 later in the day, identical to AERONET.

379 Moving from the sonde release to the whole period shown in Fig 4, the above description of the
380 thermodynamic and aerosol state of the atmosphere holds for the day. Clouds and precipitation
381 are clearly visible in the aerosol backscatter color scales as dark red (backscatter $> 10^{-4} \text{ (m sr)}^{-1}$).
382 Comparing aerosol backscatter with depolarization for the whole column (Fig. 4(a) and 4(b)),
383 clouds dominated by ice are easily identifiable from liquid by depolarization values above 40%
384 (Sassen, 1991), although as discussed later in association with DC-8 observations, low
385 depolarization does not exclude the presence of ice. Large liquid water drops can also depolarize
386 the lidar signal and signify heavy precipitation, and are thus annotated on Fig. 4(a). Yellow

387 highlight boxes of interesting cloud and aerosol phenomena are marked on Fig. 4(a), with
388 corresponding enhancements of key features in Fig. 5 derived from 10 second, 7.5 m data.
389 Finally, certain cloud types are annotated including Ac, Sc, and Ci.

390 Expanding the analysis to include the early evening of the previous day, radar and satellite data
391 (Fig A.2 and A.3) indicated multiple Cbs at various states of lifecycle were within 15-30 km of
392 the UAH lidar site. Consequently, cirrus (notable by its high depolarization) were detected
393 through Aug 12, 2013 7:00 UTC (2:00 CDT) with “bases” for virga or ice falls between 8 to 13
394 km, or -35 to -57°C. Given that homogenous ice nucleation can begin at -37°C, except in the
395 most extreme conditions, at these temperatures water tends to be ice (Pruppacher and Klett,
396 1997; Campbell et al., 2015). Virga is observed at cloud bases at ~4.5 and ~8.5 km MSL,
397 highlighted in Fig. 5(a). Using depolarization, we can see the upper cloud at 8.5 km and -25°C
398 has ice virga emanating from super-cooled liquid water in classic Ac fashion. The cloud base at
399 4.5 km and 0°C is entirely liquid by lidar observation, although we expect mixed phase processes
400 at work above where the lidar beam was attenuated. This behavior in combination with local
401 NEXRAD radar data suggests this lower cloud feature is stratiform precipitation from the anvil
402 of a decaying system.

403 In the morning of August 12 until just after daybreak (sunrise ~13:05Z; 6:05 CDT), a strong
404 aerosol return was visible centered on the 1-1.5 km MSL/0.8-1.3 km AGL range, likely a residual
405 layer from the previous day’s PBL mixed layer (ML, to 1.2 km), or entrainment zone (EZ, ~2.5
406 km). This residual layer may have been transported from the east, but also may be a result of
407 nighttime cooling and enhanced relative humidity and particle hygroscopicity. Morning
408 Stratocumulus are embedded in this layer and small liquid water Ac cloud returns are also visible
409 in the morning (inset box Fig. 5 (b)), at 5:00 UTC at ~6 km (-7°C), 10:00 UTC 4 km (5°C), with
410 the strongest returns at the 4.7 km 0°C melting level at 12:00 UTC. These clouds likely originate
411 from convective detrainment of water vapor, such as from melting level detrainment of
412 convection (e.g., Fig. 1(a) & (b)) or from the tops of TCU clouds, sustained by cloud cooling.
413 Associated with these clouds are clearly visible individual pockets of aerosol particles on the
414 order of a few hundred meters high and 15-30 minutes in duration. With backscatter returns on
415 the order of 1 to 5×10^{-7} (m sr)⁻¹, such features are <5% of Rayleigh backscatter and demonstrate

416 the Ac are embedded in larger aerosol features. At wind speeds of $5\text{-}10\text{ms}^{-1}$, these pockets are
417 between $\sim 5\text{-}20$ km wide.

418 In the early morning hours, local time, tenuous clouds are also observed at 1 km within the ML
419 residual layer, likely nighttime radiatively driven Sc. By local daybreak, CuHu begin to more
420 systematically form at ~ 1 km due to solar heating at the surface, with cloud base heights
421 increasing to 1.5 km as the ML and PBL develop throughout the morning to early afternoon LST
422 (inset Fig. 5 (c)). Clouds also formed at daybreak at 1.5 km inside a PBL residual aerosol layer.
423 At this height, above the CuHu, these clouds are decoupled from surface forcing and are
424 optically thin suggesting they are Ac, even though they share their initial formation physics with
425 Sc earlier in the day. More interestingly, a second Ac deck formed shortly thereafter, with 2-2.5
426 km MSL bases that increased in height with time through the morning to a maximum height of
427 3.7 km (5.5°C), collinear with the depth of the mixed layer. These are highlighted in inset box
428 Fig. 5(c). Based on geostationary imagery, and as demonstrated in the comparison of Fig. 2(a) to
429 (b), these clouds evaporated at noon local time, presumably under solar radiation. This situation
430 is similar to the case of Fig. 1(f). Interestingly, aerosol layers between the PBL clouds and the Ac
431 are also visible forming late morning at $\sim 15:30$ UTC, and increasing with height with the
432 developing PBL and the Ac clouds above. Cirrus also begins to advect over the site by afternoon,
433 largely detraining from thunderstorms to the north and west (Fig. A2 (b)).

434 By 23:00 UTC, a mature phase Cb spawned by the outflow of the storm sampled by the NASA
435 DC-8 4-5 hours earlier arrived at Huntsville, bringing showers to moderately heavy rain. The
436 remnants of the storm extend through the next day, producing Ac visible from August 13, 0:00
437 to 3:00 UTC between the 4.5 km melting level and 7 km (-12°C) and (Fig. 5(d)). These clouds,
438 most likely local in origin, are often categorized as convective debris Ac by the forecasting and
439 aviation community-an indicator of multi-level detrainment in the convective environment. An
440 aerosol layer exists to approximately the 4.5 km 0°C melting level capped by Ac. Additional Ac
441 exist above these embedded in faint but clearly visible aerosol layer features. Unlike the aerosol
442 pockets earlier in the day, these features are much more limited in extent, no more than 200-300
443 m in depth.

444 As the PBL collapses during the evening, it leaves a 1 km AGL residual layer not unlike those
445 present a day earlier. A final set of light showers from a decaying system occurs after the early

446 morning of August 13 at 7:30 UTC (Fig. 5(e)). With another clear melting level visible in the
447 depolarization data, this is likely residual stratiform precipitation like at the beginning of the time
448 series. Similar to the beginning of the time series, ice precipitation from super-cooled liquid
449 water clouds was also present.

450 **5.0 Results II: DC-8 Observations of an August 12, 2013 storm outflow**

451 The HSRL gives an excellent depiction of the overall aerosol backscatter and cloud phase over
452 the course of the day, but it lacks the ability to provide microphysical and chemistry information
453 on the aerosol particles themselves. For this purpose, we utilize measurements on the DC-8 that
454 flew in the region on this day. The flight pattern on August 12th included a curtain wall over the
455 Gulf of Mexico, sawtooth transit to a curtain wall over northeastern Alabama, and more sawtooth
456 patterns to a spiral on the downwind side of deep convection developing over the northwestern
457 corner of Alabama. This last maneuver in northern Alabama is marked on Fig. 2(b), and provided
458 the day's only complete tropospheric profile. Being on the downwind side of the storm's
459 trajectory, this profile also gives a snapshot of the aerosol environment detraining from an
460 isolated storm being fed by a polluted boundary layer. As the storms later passed over
461 Huntsville, observations collected by the DC-8 also provided context for the UW HSRL lidar
462 observations described in Section 4. Fig. 2 includes forward and nadir images of the overall
463 environment. However, the most representative depiction of the midday to early afternoon
464 environment is provided in Fig. 2(e), taken at 10 km altitude just as the DC-8 started its return
465 from sampling the storm. The region had a deck of CuHu and Cu with bases at 1.4 km MSL/~1.2
466 km AGL, delineating the PBL's mixed layer from its entrainment zone. As mentioned, the PBL
467 top was more ambiguous, and is functionally defined by the tops of these clouds at ~2.5-4 km
468 (e.g., Fig. 2(a)). TCu were observed, overshooting above the 0°C level, as were scattered Cbs
469 with tops at ~12-13 km. Ac were prevalent on the horizon, detraining both from overshooting
470 TCu and midlevel of Cbs.

471 Profile variables collected by probes on the DC-8 during the spiral initiated at 19:10:30 are
472 provided in Fig. 6. Included are (a) temperature and dewpoint (of liquid water) and tracer species
473 (b) ω_v and CO and (c) CO₂ and SO₂. To depict particle scattering (d) provides the DC-8 total
474 ambient 550 nm light scattering and a parallel dry light scattering for fine particles (<1 μm). For
475 context also included on Fig. 6(d) is the inferred light extinction derived from the UW HSRL by

476 assuming a lidar ratio of 55 sr^{-1} . The period of averaging for the HSRL data is 19:00-21:00 UTC,
477 or essentially from the start of the profile until just before the storms passed overhead. Total
478 particle counts from the LAS and CN counters are plotted on Fig 6(f). To prevent any possible
479 cloud water or precipitation shattering effects on the aerosol instruments, CN, nephelometer, and
480 LAS data were heavily cloud screened with data points removed for one second before the
481 arrival and two seconds after the exit of any cloud with $\text{LWC} > 0.005 \text{ g m}^{-3}$. Finally University of
482 Colorado aerosol mass spectrometer organic material and sulfate is provided in Fig. 5(f). Only
483 under very heavy ice content conditions does AMS data need to be expunged from the profile. To
484 reduce noise, a 5 second boxcar average was applied to the particle counter and AMS data. Also
485 to improve readability of PBL features, similar plots from 0-4 km are likewise included as Fig.
486 6(g)-(l) respectively.

487 The DC-8 profile depicts intricate layering behavior throughout the free troposphere in a fashion
488 consistent with the UW HSRL backscatter. As expected, the temperature profile is largely moist
489 adiabatic $\sim 6^\circ \text{ C km}^{-1}$, indicating an atmosphere that has been modified by convective processes.
490 Moist layers, well depicted in the dewpoint sounding when it converges with temperature, often
491 coincided with minor temperature inversions. For reference, these layers associated with
492 dewpoint depressions $< 2^\circ \text{ C}$ are labeled on Fig. 6 as lines, or for three deeper layers, shaded
493 bands. Characteristics of these layers are also provided in Table 1, and Fig. A.4 provides images
494 taken from the DC-8's forward video for visual context of the environment being sampled. As
495 expected, moist layers coincided with increases in ω_v . However these layers also strongly
496 coincided with increases in other trace species such as CO and dry aerosol concentration. In the
497 following subsection, we provide a narrative starting with layers influenced by PBL detrainment
498 (PBL layers 1 and 2; Sec. 5.1) followed by upper free troposphere detrainment by the Cb (UT
499 layers 1-4; Sec. 5.2). Emphasis will then be placed on the nature of aerosol and Ac layers in the
500 middle free troposphere (MT Layers 1-3; Sec. 5.3). Finally we will examine composition and
501 particle properties between these layers (Sec. 5.4).

502 5.1 PBL Detrainment Layers

503 Our first area of examination is of detraining aerosol layers associated with the development of
504 the PBL, with clouds ranging from CuHu to Cu and the occasional congestus. This baseline PBL
505 environment is described in detail in Reid et al., (2017), and is the subject of a subsequent paper

506 on particle transformation and inhomogeneity within the PBL. Here, we consider a few specific
507 aspects of the DC-8 data set to aid in overall profile interpretation, and also in the analysis of
508 covariability among aerosol, water vapor and Ac cloud formation in the middle troposphere.

509 To begin we examine the nature of the PBL's mixed layer as this is the "source" of the
510 atmospheric constituents being convectively lofted. However, the observation of the PBL's
511 mixed layer profile at the bottom of the profile is contrary to what one would expect. Most
512 notably, gas tracers such as ω_v CO, CO₂, SO₂ and particle properties are not constant with height
513 near the bottom of the profile. Based on forward video (Fig. A.3 (a)), the spiral was initiated
514 below cloud base and thus we are confident this sample is indeed in the mixed layer. Indeed,
515 there was a strong gradient in ω_v on approach to the spiral; in fact isolated showers were seen
516 across the horizon. It is therefore likely that the mixed layer is influenced by regional gradients-
517 a recurring problem with profiling with large and fast moving research aircraft.. These gradients
518 are good indicators of significant spatial variability of atmospheric constituents in the mixed
519 layer. Using a single point at the top of the mixed layer just before ascent as a baseline (Table 1),
520 ω_v and CO were at a maximum of the profile at 15.5 g kg⁻¹ and 110 ppbv, respectively. CO₂ was
521 elevated to ~190 ppbv and SO₂ 225 pptv. CN was at 2300 cm⁻³, and a LAS volume concentration
522 of 2.8 μm³ cm⁻³ for an index of refraction of polystyrene spheres, (n=1.55), consistent with AMS
523 concentration of particulate organic matter and sulfate of 4.2 and 1.5 μg m⁻³, respectively. The
524 ratio of increased light scattering due to hygroscopic growth from 20-80% RH was 1.62, typical
525 of the region (Wonaschuetz et al., 2012).

526 Within the nearest level to the surface (PBL Layer 1 in Fig. 6, ~1.6 km MSL, 1.4 km AGL) is a
527 clear aerosol enhancement just at and above mixed layer top which we diagnosed at ~1.5 km
528 through a combination of water vapor and temperature and visual inspection of cloud base from
529 the forward video (Fig. A.4). An enhancement is expected in ambient scattering at the top of the
530 mixed layer due to the increases in humidity (80% at mid mixed layer and reaching ~90%
531 between clouds) with height in the mixed layer coupled with aerosol hygroscopicity. But just
532 above the mixed layer there is an increase in CO, CO₂, dry aerosol mass, number, CN and
533 scattering. SO₂ values were exceptionally high, reaching off the plot scale to 300 pptv, indeed
534 suggesting strong compositional spatial inhomogeneity on the region. This, like the mixed layer
535 variables, might be a combination of an aliased signal, but also is influenced by detrainment

536 from the Cu clearly present (Fig. A.3(b)). At Huntsville at the same time as the DC-8 spiral, the
537 unaliased HSRL profile showed classic increased aerosol backscatter (and presumed extinction)
538 to a maximum at a level of 2 km MSL, indicating the top of the mixed layer and cloud base
539 slightly higher than the spiral location. PBL layer 1 is made up of simultaneous spikes within ω_v ,
540 CO, dry light scattering, LAS and CN concentrations, and AMS sulfate as the DC-8 passed
541 through the top of the mixed layer and into the level of the lowest cloud bases (~1.5km AGL;
542 Fig. A.4 (b)). Also was a likewise spike in SO₂. Although not shown, NO₂ spiked to mixed layer
543 levels (10's-> 100s of ppbv), and a minor dip in ozone. (40->37 ppbv). This enhancement is
544 presumably through the detrainment of mixed layer air via the fair weather cumulus. Dramatic
545 increases in CN and sulfate in particular suggest that this layer potentially hosted secondary
546 particle mass production via detrainment from nearby shallow clouds (e.g., Wonashuetz et al.,
547 2012). Although RH values were on the order of 85-90%, both the probe data and visual
548 inspection of the video data show this peak is not associated with any form of cloud
549 contamination. Ultimately, evidence suggests that this layer is detrainment of mixed layer air
550 from small cumulus. Even though this location near the Tennessee River hosts some sporadic
551 industry on its shores, the nature of the tracers, such as water vapor and CO, demonstrates this
552 layer was convectively transported from above the mixed layer by small Cu. Recent studies
553 suggest that the oxidation of SO₂ to SO₄⁼ in such clouds can be extremely fast (e.g., Loughner et
554 al., 2011; Eck et al, 2014; Wang et al., 2016).

555 The second layer analyzed, PBL layer 2, was much deeper than the first, at 2.5-3.2 MSL (Fig.
556 A.3 (c)). This layer can be classified as the upper portion of the PBL entrainment zone, where air
557 is actively mixing with the free troposphere above via detrainment from cumulus. The ω_v is
558 enhanced and, between clouds, relative humidity ranged from 80-90%. At times enhancements
559 existed in LAS particle number and in AMS sulfate and OC. Spikes in CN concentration reached
560 10,000 cm⁻³, likely a product of convective boundary layer precursor emissions receiving high
561 actinic flux not only directly from the sun, but also reflected from nearby clouds (e.g., Radke and
562 Hobbs, 1991; Perry and Hobbs, 1994; Clarke et al., 1998). As then expected, SO₂ was
563 diminished. During the DC-8's transit of this layer was a 15 second Cu penetration that included
564 significant precipitation, although this period is expunged from the aerosol particle counter
565 record in Fig. 6. In the middle of this cloud, CO reached 80 ppbv, indicating convective lofting
566 of mixed layer air. It is this cloud that we believe developed into the CB sampled. At the time of

567 this first penetration, from visual inspection, the cloud top could not have been more than ~1 km
568 above the aircraft (Fig A.4 (c)), consistent with it not being picked up with NEXRAD.

569 The PBL Layer 2 detrainment environment is discussed in detail in Reid et al. (2017), and owing
570 to convective pumping and cloud processing of mixed layer air and high relative humidity
571 contributes significantly to regional AOD variability. Sometimes described as cloud halo effects
572 to explain covariability in cloud fraction and AOD, this PBL Layer 2 is actually a wide spread
573 detrainment induced layer (Reid et al., 2017). This layer was visible not only on the DC-8
574 nephelometer and AMS data, but is also coincident with a strong aerosol return from the
575 Huntsville lidar, some ~100 km to the west. Notably, the top of this layer coincides with the
576 lifting aerosol layer topped by Ac clouds in UW-HSRL (Fig 1(f), Fig 3(a) and Fig 4(c)) and
577 serves as a potential boundary between the PBL and free troposphere.

578 5.2 Upper Free Troposphere

579 Moving from PBL influenced aerosol layers, we now briefly examine the region dominated by
580 convective outflow from the anvil, diagnosed as detrainment in association with ice. This altitude
581 domain is largely outside the scope of this paper, and will be discussed in detail in other
582 SEAC⁴RS papers. Nevertheless, for completeness a brief description is provided here. Like the
583 top of the PBL, the bottom of the cirrus anvil outflow layer is ambiguous. From Fig. 4 and in
584 particular Fig 5(a), it is clear that liquid water could exist as high as 8.5 km, or ~ -21 °C,
585 although ice was clearly nucleating and falling below this liquid water. The first full ice layers
586 were experienced by the DC-8 at 8 km and 8.4 km (UT 1 and 2, Fig A.3 (g) and (h)) followed by
587 a second cirrus cloud (UT2) a third at 9.4 km (UT3; Fig A.3 (i)), and finally a deep cirrus
588 penetration from 10-11 km (UT4; Fig A.3(j)). Because cloud particles in these layers were
589 entirely made of ice, with ice water content approaching 1 g m⁻³, aerosol size and scattering data
590 are not available; although prominent peaks in CO, sulfate, and particulate organic matter are
591 found at each level indicating convective pumping and detrainment. SO₂ showed varied positive
592 and negative correlations with these layers, suggesting perhaps varying influences of the
593 background and directly detrained airmasses. From an aerosol point of view, it is obvious that
594 significant enhancements in particle mass and number exist on either side of the cirrus layer.
595 Notably the boundaries of these layers were enriched in organics relative to sulfates, and CN>10
596 nm concentrations were on the order of 10,000-20,000 cm⁻³, particularly above 9.5 km. Indeed,

597 observations suggest that deep convection is highly efficient at transporting boundary layer air
598 through to the anvil (Yang et al., 2015).

599 5.3 Middle Free Tropospheric Layers

600 The focus of this paper is on the middle tropospheric detrainment layers, bounded below by the
601 primary PBL detrainment layer and its associated Ac clouds and above by the anvil cirrus, both
602 described above. Within the middle troposphere there were numerous perturbations in water
603 vapor, trace gas, and aerosol features. In particular, three coincident water vapor, CO and aerosol
604 layers were observed in the DC-8 spiral, clearly associated with liquid water clouds (MT Layers
605 1, 2, and 3; Fig A.4 ((d), (e), (f)). Starting from the bottom of the free troposphere and working
606 upwards, a slight inversion at 4.1 km delineated a rather minor water vapor and aerosol layer
607 (Fig. 6 MT1; Fig. A.4 (d)), which, like Layer PBL2, spanned both the DC-8 profile and the UW-
608 HSRL lidar at Huntsville. The inversion associated with this layer was a 200 m deep area having
609 a near constant temperature of 3.4°C. Visual inspection of video data suggests this level was
610 associated with the maximum heights of the larger Cu and likely represents the very top of
611 convective pumping by larger boundary-layer clouds (Fig. A.4(d)). Such an interpretation is also
612 consistent with this layer delineating a drop in aerosol light scattering and mass which has likely
613 detrained from these larger clouds. Yet coincident with this inversion is a small spike in particle
614 number, as measured by the CN counter. The similarity of this layer to PBL2 is noticeable, even
615 if ejections are more sporadic than the smaller and more numerous cumulus clouds in the region
616 that define PBL2. These layers may be isolated, or be associated with a more organized region,
617 but they nevertheless show the lofting of mixed layer air into the free troposphere. Indeed, this
618 layer reminds us that in convective environments the physical top of the PBL is difficult to
619 define; the boundary between the cloud tops and the free troposphere is variable.

620 Special attention is paid here to the next two layers (MT2 and MT3) where significant
621 perturbations to trace gas and aerosol loadings were associated with thin Ac cloud decks. Within
622 MT2, a strong aerosol return was present at 4.6 km associated with a shelf cloud deck at ~0.5°C
623 detraining from the sampled Cb (Fig. 2(d) and Fig. A.4 (e)). Most notably, MT2 layer also
624 showed the strongest positive perturbations for ω_v , CO, CO₂ and a minimum in SO₂. This
625 suggests that air from this layer was largely from the boundary layer with its SO₂ scavenged.
626 MT3 contained a deeper layer of isolated Ac clouds from ~6 to 7 km (-6 to -12°C; Fig. A.3(f)).

627 These layers are similar in nature to layers observed throughout the day at Huntsville (e.g., Fig.
628 5(b) and (d)). Detailed time series of data as the DC-8 passed through these two layers are
629 presented in Fig. 7.

630 MT2 at 4.6 km was targeted for direct penetration by the DC-8 because it represented a classic
631 melting level Ac detrainment shelf commonly observed around the middle of Cbs (e.g., Fig. 1(a);
632 Johnson et al., 1996; Posselt et al., 2008). The DC-8 approached the cloud from the side at a
633 slow climb rate ($\sim 1 \text{ m s}^{-1}$), and flattened out for Ac cloud sampling, followed by a more
634 accelerated climb (Fig. 7(a)). Consequently, the DC-8 captured the environment below and to the
635 side of the Ac deck, and the Ac deck itself. Given the air speed of $\sim 156 \text{ m s}^{-1}$, the 50 second time
636 series for this aerosol and cloud layer spans $\sim 8 \text{ km}$. On approach, water vapor, CO, dry light
637 scattering and aerosol mass species also increased in a layer perhaps only 200 m thick. Water
638 vapor changed in a series of steps, suggesting coherent layers, including a very sharp drop in
639 water vapor for only a few seconds just before cloud penetration, only to drop again on exit. The
640 drop in ω_v and cloud liquid water was immediately below a 2°C magnitude temperature
641 inversion.

642 Aerosol particle counts for $d_p > 0.1 \mu\text{m}$ (and particle volume, not shown) also increased on
643 approach to the Ac. Total CN ($d_p > 10 \text{ nm}$) dropped precipitously, suggesting an overall shift in
644 the background size distribution in an environment that disfavored nucleation. Cloud penetration
645 lasted ~ 20 seconds ($\sim 3 \text{ km}$) and cloud liquid water contents ranged from 0.12 to 0.18 g m^{-3} .
646 Droplet effective radius from the cloud probes (not shown) was consistently in the $4.5\text{-}6 \mu\text{m}$
647 range, lower than the $\sim 8 \mu\text{m}$ values observed by Terra MODIS earlier in the day. Not
648 surprisingly, with a cloud temperature of $\sim 1^\circ\text{C}$ no ice was present. While aerosol number or size
649 distributions are unavailable during cloud sampling due to inlet shattering, CO clearly peaked
650 within 200 m of the altitude of the cloud. Yet, the AMS showed a decrease not only within the
651 cloud, but also just before cloud entry. As the DC-8 climbed up and away from the Ac deck,
652 LAS particle counts and AMS OC and sulfate dropped, while CN returned to baseline levels and
653 even spiked for a short period. Overall, MT2 observations match qualitatively what was seen in
654 the HSRL data, with the cloud resting on the top of the aerosol layer.

655 While MT2 was associated with a thin detrainment shelf, Layer MT3 was representative of a
656 much deeper layer of convective detrainment, spanning the 6-7 km level. Like MT2, there was
657 enhancement of ω_v , CO₂, CO, and a reduction in SO₂. These layers can be visualized in the
658 Huntsville HSRL data in Fig. 5 (b) and (d). Sampling of this layer was in the form of steps (Fig
659 7(g)). Throughout this layer, ω_v and relative humidity varied in such a way that this overarching
660 layer is most likely an agglomerate of many layers. The existence of several thin layers at
661 various heights may result from detrainment at the tops of terminal congestus with termina at
662 different levels (Moser and Lasher-Trapp, 2017). Consequently, very faint Ac clouds were visible
663 on the video (e.g., Fig. A.4 (f)), though there were few actual cloud penetrations. The clouds
664 sampled had very meager liquid water contents ($<0.01 \text{ g m}^{-3}$); barely clouds. Yet, these clouds
665 were mixed phase with ice clearly visible in 2D probe data at temperatures of -10° C , (Fig. A.5
666 annuluses are also ice out of focus). Under some circumstances ice habits can be indicative of ice
667 forming temperatures. However for these clouds, ice particle were over a mm in diameter, and
668 of irregular habit. There is some indication from column and hollow column habit, consistent
669 with a local freezing at -10° C and low supersaturation. But without precise temperature histories
670 this is largely conjecture. Such ice is not always noticeable in lidar data, as optics may be still
671 dominated by spherical liquid droplets.

672 For most of MT3, ω_v and CO varied in concert. However, at the very top of the level, they
673 quickly become anti-correlated-suggesting water vapor at this location is not being brought from
674 the boundary layer. Instead, it may be from entrained air along the sides-perhaps along cloud
675 edges air entraining in is the first to detrain out (Yeo and Romps, 2013). Aerosol data is not
676 much more enlightening. Aerosol mass was rather steady, and at reduced concentration than its
677 lower level counterparts. At the same time, spikes in aerosol counter and nephelometer data
678 occurred near clouds, and may just as easily be a result of droplet shattering artifact rather than
679 convective pumping.

680 5.4 Vertical Profile Aerosol Chemistry and Mass

681 Previous subsections in Section 5 describe the nature of individual detrainment layers. In this
682 final subsection, we provide a closer examination of differences in their properties. If we
683 conceptualize the environment as being influenced by shallow to deep injections of mixed layer
684 air being convectively transported to the free troposphere by clouds entraining and detraining air

685 along the way, it is best to start with reliable tracers such as CO. Fig. 8 includes profiles of the
686 ratio of aerosol number and mass to excess CO.

687 *5.4.1 H₂O and CO*

688 Paramount to all subsequent interpretation of the profile is the molar ratio of excess water vapor
689 to CO. Whereas we can take background CO value of 60 ppbv (or any nearby value as long as
690 we are consistent), water vapor is a bit more problematic. We derived excess water vapor by
691 taking advantage of the deep convection horizontal scope of several hundred kilometers upwind
692 of UAH. A background value was derived from the average mixed layer mixing ratio, followed
693 by a 4th order polynomial fit against pressure above the mixed layer ($r^2=0.99$). The calculated
694 excess ω_v between the DC-8 and UAH sounding is provided in Fig. 8(a). As expected, ω_v is
695 enhanced in the vicinity of convection, notably in the mixed layer, as well as individual PBL and
696 mid-level detrainment layers, such as 3 km (PBL2), 4.6 km (MT2, 0°C), 6-7 km (MT3). Water
697 vapor is also more broadly enhanced in the upper troposphere layers (UT1-4).

698 Moving from establishing the background water vapor profile, we next consider how a parcel of
699 air lofted into the PBL deviates from textbook descriptions during deep convection. If the parcel
700 ascends without mixing, the water vapor mixing ratio is expected to decrease with altitude, as
701 temperature decreases at the moist adiabatic lapse rate and water vapor is removed by
702 condensation and precipitation. In contrast, CO is expected to remain constant over the time
703 scale of convective ascent. In reality, the vertical profiles of both constituents are modified by
704 entrainment/detrainment processes, and theory and numerical experiments indicate there are few
705 truly undiluted parcels to be found anywhere in regions of shallow or deep convection (Zipser
706 2003; Romps, 2010; Romps and Kuang, 2010). Parcels that ascend in a region near the core of
707 convection (far from the cloud edge) may conserve CO and approximately follow a moist
708 adiabat. Parcels closer to the cloud top and edge will undergo mixing with air that has originated
709 from various levels inside and outside of the cloud, and may reflect multiple entrainment-
710 detrainment events (Yeo and Romps, 2013). The ratio of water vapor to CO concentration in
711 undiluted ascent should be uniquely determined by the parcel's initial properties in the mixed
712 layer, and departures from this ratio within the cloud reflect the action of mixing. Outside of the
713 cloud, the situation is a bit more complicated. We expect water vapor content to decrease with
714 height, and, if CO is well mixed, then the concentration will be constant with height. Increases in

715 the ratio of water vapor to CO with height reflect the action of detrainment from convection, as
716 water vapor decreases with height more rapidly than CO.

717 The 0°C melting level is further related to the air parcel characteristics. The molar profile of
718 excess H₂O to CO ratio is provided in Fig. 8(b), and throughout the lower troposphere the ratio
719 increased to a maximum at the 0°C melting level. This increase reflects a more rapid decrease in
720 CO with height relative to water vapor, and is punctuated by two local maxima in the ratio at 1.5
721 km and 3 km above the surface. Above the melting level, the ratio of H₂O to CO precipitously
722 drops, then exhibits local maxima at 5 km and 5.5 km.

723 Examining possible causes of the water vapor and CO ratio variability in the vertical above the
724 0°C melting level entails a closer examination of the impacts of detrainment on an air parcel.
725 Detrainment of air from convection results in local increases in both water vapor and CO;
726 however, water vapor content in detrained air will be greater than CO due to evaporation of
727 cloud condensate. The general increase in water vapor to CO ratio indicates the repeated action
728 of entrainment/detrainment and evaporation of cloud condensate around developing cumulus
729 clouds, while local maxima in water vapor to CO ratio reflect the action of enhanced detrainment
730 at specific levels; in this case, the tops of CuHu and Cu at 1.5 and 3 km, respectively. Detraining
731 air from congestus and deep convection at the melting level provides the strongest local source
732 of water vapor (direct and via evaporated cloud), and also the largest water vapor to CO ratio.

733 Contrary to the spikes in water vapor content caused by detrainment, immediately above the
734 melting layer, water vapor content is very low as this air originates in the middle and upper free
735 troposphere (c.f., Figs. 4 and Posselt et al. 2008). CO consistently remains relatively high, since
736 CO is relatively well mixed in the middle and upper free troposphere (Fig. 5b). The near
737 discontinuity in water vapor content in the vertical, coupled with relatively small changes in CO,
738 result in the rapid decrease in water vapor to CO ratio above the melting layer. Relatively high
739 CO concentrations in the air detrained at and below the melting layer can be seen in the profile of
740 CO (Fig. 5b) and in the aerosol number to CO ratio maxima in Fig. 7b. Above the melting layer,
741 such as in the 6-7 km region (MT #3) thin layers of high water vapor to CO ratio are likely due to
742 detrainment from Cumulus congestus clouds.

743 *5.4.2 Aerosol Mass*

744 Moving to aerosol particle profiles, different aspects of convective transport reveal themselves.
745 The ratio of LAS particle concentration ($d_p > 0.1 \mu\text{m}$, representing the accumulation mode) and
746 CN ($d_p > 10 \text{ nm}$, representing the nucleation mode) to CO is presented in Fig. 8(c). Relative to
747 CO, accumulation mode particles largely drop continuously in number from the surface to 0°C
748 level. Positive perturbations exist within the PBL and MFT aerosol layers as diagnosed in Fig. 6.
749 At heights above the 0°C level, the accumulation mode to CO ratio stabilizes at lower
750 concentrations with occasional layers. There is some difference in light scattering (Fig. 8(d)) and
751 OC and sulfate from the AMS ((Fig. 8e)), where we find mass enhancement in the PBL
752 detrainment zone.

753 Nucleation mode aerosol becomes more prominent with height owing to more intense solar
754 radiation and a decrease in available accumulation mode surface area. Nucleation rates of
755 particles from precursor detrainment from anvils can be rapid (Waddicor et al., 2012).
756 Detrainment layers host strong positive and negative perturbations in CN count, which do not
757 project significantly onto light scattering or mass. This is in contrast to the concentration of
758 accumulation mode particles which do project strongly onto optical observables.

759 To explore variability in particle size distributions in the vertical, Fig. 9(a) and (b) provide LAS
760 number and volume size distributions for key levels throughout the profile, and is consistent with
761 what can be inferred from Fig. 8. Best fit baseline particle size distribution within the mixed
762 layer suggest Count Median Diameter (CMD) and Volume Median Diameter (VMD) of $0.14 \mu\text{m}$ and
763 $0.25 \mu\text{m}$, respectively. At the first layer (PBL 1), dry particle size CMD and VMD increases to
764 $0.16 \mu\text{m}$ and $0.28 \mu\text{m}$, respectively, at the same time of increases in particle mass relative to CO.
765 This is all consistent with secondary aerosol particle mass production on existing particles. After
766 this point, we find a reversal in particle CMD and VMD with height. This is suggestive of
767 precipitation scavenging of larger particles in larger clouds the deeper the detrainment. That is,
768 particles that are detraining from smaller non-precipitating clouds keep their secondary produced
769 mass. However these same aerosol particles that grow to larger sizes are more likely to be lost to
770 droplet nucleation and scavenging. Nevertheless, significant aerosol mass from the boundary
771 layer still is ejected in the anvil as evidenced in the 9-11 km altitude range in Figs 8 (d) and (e).

772 5.4.3 OC and Sulfate

773 The 0°C level is clearly a delineator in the sulfate to OC ratio (Fig. 8(f)). Near the surface the
774 ratio of sulfate to OC is ~0.4. In the first PBL detrainment layer (PBL1) there is a doubling of
775 sulfate relative to CO. Such a mass increase relative to CO may be indicative of secondary
776 aerosol production-and indeed sulfate peaks in this layer not only against CO, but also relative to
777 OC (Fig. 7(e, f)). Particulate organic matter mass relative to CO peaks in PBL Layer 2, but with a
778 reduction in sulfate. Detrainment from this layer is associated with deeper clouds, including
779 warm precipitating clouds in the immediate vicinity. Thus, sulfate particles may be preferentially
780 scavenged.

781 The ratio of sulfate to OC further changes systematically through the profile, decreasing to a
782 minimum just below 4 km. This, coupled with the decrease in accumulation mode number
783 relative to CO, may be a further indicator of aerosol particle processing and scavenging in
784 clouds. Indeed, the mid-troposphere layers that show a reduction in SO₂ do see an increase in
785 sulfate. Above 4 km, sulfate increases again, perhaps due to oxidation of residual interstitial or
786 dissolved but unoxidized sulfur species in either Ac clouds or in gas phase. This increase may
787 also be related to the relative mass distribution within detraining cloud droplets. Sulfate mass
788 fractions do appear to recover in the upper troposphere, perhaps due to homogenous nucleation
789 of the small amount of SO₂ detraining from sublimating ice. However, we cannot exclude this
790 high number of nucleation mode particles as being part of the regional background.

791 **6.0 Discussion I-combining datasets and hypothesis development**

793 The purpose of this paper is to demonstrate on a canonical day that aerosol layering
794 characteristics in the free troposphere and PBL entrainment zone are delineated by cloud
795 structure and its associated thermodynamic profile. Examination of this day leads to many
796 questions about aerosol processes and potential impacts or feedbacks with understudied Ac
797 clouds. To help the field progress, in this section we use the combined datasets from the UW
798 HSRL and the DC-8 aircraft to formulate several hypotheses about Ac formation that need
799 further attention by the community.

800 6.1 Hypothesis: Ac cloud's low liquid water and slow updraft velocities are susceptible to small
801 changes in the CCN population

802 One of the most remarkable aspects of next generation lidar systems such as the UW HSRL used
803 here and the new Raman systems such as described in Schmidt et al., (2015) is their ability to
804 observe intricate aerosol features at very low particle concentrations. Fig. 3(d), 4 and 5
805 demonstrate fine coherent structure of aerosol layers in the free troposphere that, in the past,
806 were rarely quantified. Even with aerosol backscatter levels at or even under $<5 \times 10^{-8} \text{ (m sr)}^{-1}$, or
807 $<5\%$ of Rayleigh backscatter, aerosol layers of only a 100 to a few 100 meters thickness are
808 clearly visible. These thin aerosol layers can persist for hours, undergoing gravity wave
809 undulations along with gradual changes in observed layer height at the meso- to synoptic scales.
810 Ac are often associated with observed aerosol layers, and the clouds we observed had very low
811 liquid water contents of a few tenths of a g m^{-3} at most (e.g., Fig. 7). Drawing from parallels to
812 Sc (e.g., Martin et al., 1994; Platnick and Twomey 1994; Ackerman et al., 1995; to most recently
813 Wood et al., 2018), or the very limited available measurements of such relationships for Ac in the
814 field (e.g., Reid et al., 1999; Sassen and Wang, 2008; Schmidt et al., 2015), we would expect Ac
815 clouds' low liquid water and slow updraft velocities to result in strong effective radius sensitivity
816 to CCN populations. Indeed, Ac have characteristics very much like Sc (e.g., Heymsfield et al.,
817 1991; 1993), and critical supersaturation can be reasonably well calculated for Sc and Ac (e.g.,
818 Snider et al., 2003; Guibert et al., 2003). Given the importance of solar radiation to cloud
819 lifetime (e.g., Larson et al., 2001; 2006; Falk and Larson, 2007) it stands to reason that aerosol-
820 Ac sensitivities can then project onto cloud reflectivity, cloud lifetime and consequently the local
821 energy budget. Quantifying this balance of different terms influencing the parcel lifecycle remain
822 a challenge (e.g., Falk and Larson et al., 2007).

823 Nevertheless in global aerosol populations that have strongly varying signals regionally, (e.g.
824 Alfaro-Contreras, et al., 2017) may result in large scale trends in Ac cloud cover (e.g.,
825 hypotheses by Parungo et al., 1994) and reflectivity. However estimating CCN concentration
826 based on the regional aerosol loading is a difficult task. One is attempting to estimate the
827 properties of a very thin aerosol layer with highly complex relationships to the boundary layer
828 and regional convection using likewise complex microphysics in highly variable and at times
829 weakly forced clouds. This is discussed further in Section 7.

830 6.2 Hypothesis: CN events can sustain and enhance CCN populations in Ac clouds

831 The impact of aerosol dynamics of the region must be considered when addressing a number of
832 science questions. Aerosol backscatter is dominated by accumulation mode particles that, owing
833 to their size, also make the best CCN. While there are copious CN, there are few particles in
834 number of any appropriate size to behave as CCN ($\sim 100 \text{ cm}^{-3}$ or less in the LAS at altitudes
835 above the 0°C level). Considering the proclivity of CN nucleation events, and the overall
836 increasing numbers of CN at higher altitudes, the CCN versus optical detection relationship is
837 complex, (e.g. Schmidt et al., 2015), especially if one considers homogenous nucleation and
838 processing (e.g., Perry and Hobbs., 1994; Kazil et al., 2011). Enhancements in accumulation
839 mode particles near Ac appear to be anti-correlated with CN for this case-likely due to available
840 surface area for secondary mass production and or coagulation. At the same time, explosive
841 nucleation events are visible and expected. This all leads to questions about layer flow dynamics
842 in and around Ac and their associated aerosol layers and/or halos. Does the cycling of air through
843 an Ac feedback into its own CCN budget? Does non-precipitating cycling enhance particle size
844 and hence CCN number for any given supersaturation? In precipitating Ac, where are
845 replacement CCN coming from, and do nucleating CN ever offer a supply? Or, as a hypothesis,
846 perhaps CN events can sustain and enhance CCN populations in Ac clouds. The null hypothesis
847 would then be that CN are consumed in individual droplets and have little overall effect in clouds
848 with such meager updraft velocities and super saturations. This topic in particular needs to be
849 addressed in highly detailed modeling studies.

850 6.3 Hypothesis: At and below the melting level, air is dominated by detrainment of boundary
851 layer air and above the melting level in the middle free troposphere, air is more influenced by
852 entrainment and detrainment along the cloud edges. However PBL air can be ejected through the
853 anvil.

854 This hypothesis or ones like it is related to the fundamental “plumbing” of convection and what
855 fraction of air from which levels is transported where. Much of the combined Ac/aerosol
856 environment rests on the nature of convective detrainment and this detrainment phenomenon
857 may give insight into cloud dynamics and transport. The updraft core is somewhat insulated from
858 entrainment/detrainment processes, whereas parcels closer to the cloud top and edge will
859 undergo mixing with air that has originated from various levels inside and outside of the cloud.
860 Observations around clouds may reflect multiple entrainment-detrainment events (e.g., Yeo and

861 Romps, 2013). The ratio of water vapor to CO concentration in undiluted ascent should be
862 uniquely determined by the parcel's initial properties in the mixed layer, and departures from this
863 ratio within the cloud reflect the action of mixing. Detraining air from deep convection at the
864 melting level provides the strongest local source of water vapor (direct and via evaporated
865 cloud), and also the largest water vapor to CO ratio. We hypothesize that, up to and including the
866 melting level, detrainment is dominated by boundary layer air, whereas above this level air is
867 more influenced by entrainment and detrainment along the cloud tops and edges. Indeed, for the
868 melting level shelf the significant combined enrichment of CO and CO₂ is perhaps the strongest
869 evidence that air detraining from this level is from the boundary layer which presumably was
870 from the core of the cell. It is noteworthy also that the Ac cloud observed on the DC-8 was not
871 directly at 0°C, but rather 0.75°C, consistent with the formation of an inversion directly above it
872 (e.g., Fig. 7(b), T minimum not exactly at 0°C, but rather at 0.5°C). These observations are in
873 agreement with the simulations by Posselt et al., (2008) and Yasunaga et al. (2008), both of
874 which were modeling studies that managed to form melting level clouds without any predefined
875 environmental area of stability. Perturbations in temperature may be representative of large scale
876 vertical motions on the outside of the clouds, including downdrafts adjacent to regions of in-
877 cloud upward motion. Schmidt et al., (2014) suggested that the heating/cooling differentials in
878 the vicinity of altocumulus clouds can result in areas of mesoscale subsidence, further perturbing
879 flow fields and presumably CCN intake into these clouds.

880 We leave open the possibility that depending on storm dynamics, parcels in the inner core of
881 convection can be ejected into, and out of, the anvil. This overall structure, with PBL air at cloud
882 tops and bottoms, with more entrainment/detrainment dominated properties is supported in Fig. 8
883 where aerosol mass ratios to CO are given as well as an altitude dependence of sulfate to organic
884 matter is given. So clearly different altitude ranges have strong relationships to cloud
885 entrainment and detrainment processes and the overall convective structure. Models can certainly
886 provide insight, but considerable thought must be given to verification.

887 **7.0 Discussion II: Water vapor, aerosol and altocumulus layer observations in the** 888 **context of radiative balance and climate change.**

889 As elucidated in the introduction, Ac clouds do not garner the attention they deserve relative to
890 their likely importance in the earth's radiation budget. This study demonstrates some of the key

891 challenges that the community faces in establishing an Ac budget which may discourage
892 investigation. From a remote sensing point of view:

- 893 1) Ac clouds are prevalent in the early morning hours, as well as in the vicinity of
894 convection, shielded by associated cirrus above and cumulus clouds below (Fig. 4).
895 Thus, they are likely underrepresented in cloud climatologies based on satellites,
896 particularly polar orbiting such as on Terra, Aqua, and JPSS.
- 897 2) Ac cloud layers have a significant open celled structure, with very low liquid water
898 contents and paths (e.g., Figure A.4). Combined with assumptions that underlie passive
899 remote sensing, specifically that radiation is plane parallel and cloud fields are uniform in
900 a pixel, are severely challenged by the fractus nature of these clouds. Indeed, in visible
901 wavelengths we can see that the entire Ac deck is semitransparent (Fig. 1(e), 2(a) &(h)).
- 902 3) Even under excellent viewing conditions, Ac clouds tend to exist at the same levels as
903 large Cu (Fig. 1(a), (b) & (d)). Thus, identification by single pixel IR techniques cannot
904 distinguish between the two.

905

906 At the same time, the CCN population for Ac decks are low in concentration and exist just below
907 the cloud layer. Given the difficulties in modeling aerosol entrainment and entrainment
908 processes, one might think that direct observation would be the most straightforward avenue of
909 study. To provide aerosol microphysics information, an aircraft such as the DC-8 is required. But
910 in the context of the aerosol structure highlighted in Fig 5, aircraft sampling is highly aliased.
911 This is compounded by the typical structure of a thin Ac deck above its associated thin aerosol
912 layer. Broad sampling of the free troposphere would reveal only periodic collinear perturbations,
913 and aircraft location relative to the rest of the fine aerosol structures would remain unknown.
914 Even if the DC-8 were directly over the Huntsville site, interpretation of the data would be
915 complicated by features such as gravity waves and halos around individual clouds. Based on the
916 previous discussion in Section 6, we expect Ac to be highly sensitive to changes in CCN
917 population, not only from the detrained layer, but also by layer nucleation and cloud processing.
918 Compounding the remote sensing challenges of properly identifying Ac are the system's aerosol
919 components. Clearly the proclivity of Ac to form in geometrically and optically thin detrainment
920 layers defy current satellite remote sensing capabilities for layer detection. Layer penetration by
921 aircraft is for only a few seconds, and likely disrupts the cloud field.

922 Without a doubt, more in situ aircraft operations are needed, but they need be performed in
923 conjunction with ground, airborne and space based remote sensing, particularly lidars. Indeed,
924 much of the Ac literature base surrounds lidar systems. While elastic backscatter systems
925 certainly have merit, the low aerosol signal compared to the relatively bright Ac cloud presents a
926 significant observational challenge. HSRL or Raman systems are needed in order to
927 quantitatively derive quantitative aerosol backscatter and/or extinction around such features.
928 Nevertheless, data from lidars are underdetermined. Aerosol backscatter and/or extinction, even
929 spectrally resolved, are only semi-quantitatively related to CCN concentrations.

930 The challenges the Ac system poses perhaps can be seen as an opportunity for the scientific
931 community. Just as Ac clouds are likely underrepresented in some cloud studies, Ac clouds
932 likewise disrupt other cloud studies. Certainly there are new satellite sensor concepts that can be
933 considered, such as improved lidar and radar capabilities in association with the proposed NASA
934 Aerosol and Cloud, Convection and Precipitation (ACCP) mission. But, these potentially new
935 capabilities should be taken in the context of the existing tools. For example, any Ac observing
936 strategy should include the next generation of imagers, such as on GOES-16/17, Himawari-8,
937 and Meteosat Third Generation (MTG). Higher resolution imagers with infrared capabilities
938 (e.g., Advanced Spaceborne Thermal Emission and Reflection Radiometer-ASTER; and
939 Landsat-8) or near-infrared capabilities, such as Sentinel-2 Multi-Spectral Instrument (MSI), are
940 also excellent candidates for . In the meantime, dedicated airborne measurements with imagers
941 and both aerosol and water vapor lidars can be brought to bear in short order. The Ac
942 environment also provides currently untapped potential as a relatively closed system for high
943 resolution modeling and radiative transfer. Ac layers are less than a few 100 m thick, and clearly
944 have shear flows and overturning circulations associated with them (e.g., Figure 5(b)). Study of
945 Ac layers will, as such, likely require numerical simulations run with very high vertical and
946 horizontal resolution. In addition, the potential susceptibility of Ac to changes in CCN requires
947 the use of sophisticated aerosol-aware cloud microphysical schemes.

948

949 **8.0 Conclusions**

950 This paper presents August 12, 2013 as a case study from the SEAC⁴RS campaign that
951 demonstrates Altocumulus cloud (Ac), aerosol and water vapor layering phenomena in a
952 convective regime over the southeastern United States (SEUS). This day was chosen due to

953 proximity of the DC-8 research aircraft to a High Spectral Resolution Lidar (HSRL) at
954 Huntsville, AL. The HSRL gives period level perspective on Ac clouds and their observed
955 aerosol “halo” to help interpret in situ DC-8 data. Analysis of the meteorology of the region on
956 this day supported the assertion that aerosol was “local” to the SEUS and thus should be
957 considered to be representative of regionally forced convective environments. A 33 hour sample
958 of lidar data was presented to demonstrate the diurnal cycle of cloud and aerosol features in this
959 convective environment. The HSRL provided aerosol backscatter and precisions at or better than
960 5% of Rayleigh, and demonstrated extraordinarily fine aerosol features in the vicinity of
961 altocumulus clouds formed in the outflow of deep convection. This day was in turn compared to
962 a DC-8 profile conducted that afternoon on the downwind side of a developing storm providing
963 in situ data on the middle free troposphere aerosol environment.

964 Aside from typical boundary layer development and cirrus outflow, numerous aerosol and Ac
965 decks were identified, many of these Ac produced ice virga. Ac formed at the top of the residual
966 of the previous day’s planetary boundary layer entrainment zone, where air was largely
967 influenced by boundary layer cloud detrainment. This layer formed in the morning hours, and
968 increased in base altitude with the developing boundary layer below it. Such rising may be a
969 result of mesoscale flows or cloud lofting.

970 Above the PBL-top Ac, several other combined aerosol-Ac-water vapor layers were observed.
971 Including 1) a 4 km detrainment layer that we surmise is from the very tops of cumulus
972 mediocris clouds; 2) layers just below 4.6 km/0°C melting level inversion (~ 1.5°C inversion
973 strength) representing deep convective detrainment shelves with air originating from the
974 boundary layer, and 3) 6-7 km layers that appear to be consistent with detrainment from the tops
975 of congestus clouds at the top of a layer of stability. From the HSRL and the DC-8 aerosol
976 observations, Ac clouds were associated with clear aerosol “halos”, with Ac clouds on top. The
977 intensity of aerosol backscatter associated with Ac cloud halos appeared to decrease with height,
978 beyond what would be expected from adiabatic expansion. The lowest Ac clouds associated with
979 PBL entrainment zone have larger returns associated with their proximity to the polluted PBL
980 and large accumulation particle size, and hygroscopicity. However, middle free troposphere
981 layers had markedly smaller accumulation mode sizes with height, but higher CN counts and
982 strong positive CO and CO₂. Aerosol layers above 0°C had the smaller accumulation mode sizes

983 and highest CN concentrations. This is consistent with further cloud processing and scrubbing of
984 detraining air at higher altitudes. Particle size and composition data suggest that detraining
985 particles undergo aqueous phase or microphysical transformations, while at the same time larger
986 particles are being scavenged.

987 Examination of profiles suggest an excess of water vapor and aerosol particles relative to CO
988 within and above the PBL entrainment zone to the melting level, and observations around clouds
989 may reflect multiple entrainment-detrainment events (e.g., Yeo and Romps, 2013). We expected
990 the ratio of water vapor to CO concentration in undiluted ascent should be uniquely determined
991 by the parcel initial properties in the mixed layer, and departures from this ratio within the cloud
992 reflect the action of mixing. Detraining air from deep convection at the melting level provides
993 the strongest local source of water vapor (direct and via evaporated cloud), and also the largest
994 water vapor to CO ratio. We hypothesize that up to the melting level, detrainment is dominated
995 by boundary layer air, whereas above this level air is more mixed involving
996 entrainment/detrainment along the clouds. Water vapor flux to the middle free troposphere may
997 also be enhanced by evaporating precipitation, whereas higher altitude parcels undergo
998 dehydration.

999 This work leads to numerous questions regarding relationships between aerosol layers and the
1000 properties of Ac clouds. It has been long hypothesized that increasing trends in aerosol
1001 concentrations over the past decades will result in more convective lofting, and then perhaps an
1002 indirect effect in associated Ac clouds and increases in cloud lifetimes (e.g., Parungo et al.,
1003 1994). The observation that Ac clouds have visible halos of accumulation mode particles
1004 certainly indicates that Ac are coupled with the boundary layer aerosol system. Enhancements in
1005 accumulation mode particles near Ac appear to be anti-correlated with CN for this case-likely
1006 due to available surface area for secondary mass production and or coagulation. At the same
1007 time, explosive nucleation events are visible and expected in the vicinity of clouds. All of this
1008 suggests complex CCN-Ac coupling and questions about layer flow dynamics in and around Ac
1009 and their associated aerosol layers and/or halos. Does the cycling of air through an Ac feedback
1010 into its own CCN budget? Does non-precipitating cycling enhance particle size and hence CCN
1011 number for any given supersaturation? In precipitating Ac, where are replacement CCN coming
1012 from, and do nucleating CN ever offer a supply? Or, as a hypothesis, perhaps CN events can

1013 sustain and enhance CCN populations in Ac clouds. The null hypothesis would then be that CN
1014 are consumed in individual droplets and have little overall effect in clouds with such meager
1015 updraft velocities and super saturations.

1016
1017 Finally, this study and many cited within point to a potential observational gap in Ac clouds in
1018 the observing system. Their strong diurnal cycle, low liquid water contents, stratocumuliform
1019 nature, likely makes them efficient perturbers of the radiative budget and simultaneously difficult
1020 to characterize by satellite. The field thus far has largely depended on ground based lidar
1021 systems, CloudSat-CALIPSO and isolated aircraft observations to characterize the properties of
1022 these clouds. But much more study is required, and Ac should be considered more prominently
1023 in satellite and airborne mission formulation.

1024

1025 **9.0 Author contributions**

1026 JR: Lead author and investigation; DP, KK, & RH: investigation and manuscript composition;
1027 GC, ST, CT, SW, & LZ: Flight, data, and science support; All others data providers

1028

1029 **10.0 Acknowledgements.**

1030 We are grateful to NASA Atmospheric Composition Focus Area for their sponsorship of the
1031 SEAC⁴RS campaign, as well as to all of the senior leadership, management and scientists that
1032 contributed to this successful mission. Funding for the deployment of the UW-HSRL was
1033 provided by the CALIPSO science team as a contribution to the SEAC⁴RS program. Analysis of
1034 the data presented here was provided by a NASA Atmospheric Composition Campaign Data
1035 Analysis and Modeling program (NNH14AY68I) and the office of Naval Research Code 322
1036 (N0001414AF00002). The SEACIONS network, organized at by PI Anne M. Thompson and
1037 Jacquie Witte at NASA/Goddard NASA/Goddard was initially supported through a grant to
1038 Pennsylvania State University (NASA NNX12AF05G). PCJ and JLJ acknowledge support from
1039 NASA NNX15AT96G. We are grateful to SPEC incorporated (esp. Paul Lawson) for providing
1040 cloud probe data, Jose Jimenez (University of Colorado) for providing aerosol mass spectrometer
1041 data, Andreas Beyersdorf (NASA LaRC) for CO₂ data, and Lewis Huey (Georgia Tech) for SO₂
1042 data. A portion of this research was carried out at the Jet Propulsion Laboratory, California
1043 Institute of Technology, under a contract with the National Aeronautics and Space
1044 Administration. Airborne data [doi:10.5067/Aircraft/SEAC4RS/Aerosol-TraceGas-Cloud](https://doi.org/10.5067/Aircraft/SEAC4RS/Aerosol-TraceGas-Cloud). All
1045 SEAC⁴RS DC-8 and geostationary data is available at [https://www-](https://www-air.larc.nasa.gov/missions/seac4rs/)
1046 [air.larc.nasa.gov/missions/seac4rs/](https://www-air.larc.nasa.gov/missions/seac4rs/). All HSRL lidar data used in this analysis is available at
1047 <http://lidar.ssec.wisc.edu/>. MODIS satellite data used in this mission was downloaded from
1048 <ftp://ladsweb.nascom.nasa.gov/>

1049

1050 **11.0 Appendix A. Supplemental meteorology analysis and imagery**

1051 This appendix includes a meteorological analysis of August 12, 2013 and corresponding figures
1052 to support the interpretation of this study. Fig.A.1 presents the entire DC-8 flight track for the
1053 August 12 flight, including marks for coordinated curtain wall profiles over water (1) and land
1054 (2) with the NASA ER2 and the location of the storm sampled thereafter (3). Fig. A.2 provides
1055 NEXRAD reflectivity spanning the study period, with higher temporal resolution when the DC-8
1056 was sampling the storm. Marked are the Huntsville site (red circle) and the location of the DC-8
1057 aircraft. Fig. A.3 provides GOES 13 11 μm channel images of the storm that produces Ac clouds
1058 in the Huntsville lidar data in Fig. 5(d). (a) 12 Aug 2013, 1715z highlighting PBL detrained Ac
1059 clouds. Subsequent panels show with an arrow the back trajectory location with corresponding
1060 cloud top temperatures: (b), Initiation time for the back trajectory to the 0°C cloud. (c) Ten hour
1061 back trajectory endpoint to large detrainment shelf (d) Cb that formed the AC layer. Tracking this
1062 observed layer suggests it was transported ~ 350 km. Fig. A.4 provides images from the DC-8
1063 forward video for different altitudes and layers along the DC-8 spiral. Fig. A.5 provides 2-D
1064 images of ice crystals measured in Ac clouds for the storm sampled.

1065 To provide context to this analysis, we provide a meteorological overview of the region during
1066 the early phases of the SEC⁴RS study. August 5-14, 2013 was a convectively active period over
1067 the SEUS during the summer of 2013. Weak mid-level shortwaves or cold and stationary fronts
1068 impinging on high pressure along Southern Mississippi, Alabama, and Georgia brought
1069 convective activity throughout the northern SEUS and Tennessee Valley. While scattered
1070 afternoon precipitation formed throughout the region, a stationary front on August 11 over
1071 southern Kentucky produced more substantial cells with series of southeastward propagating
1072 outflow boundaries, leading to subsequent convection over northern Alabama and Georgia
1073 through the day (Fig. A.2). One such band of Cbs passed through Huntsville in the early evening
1074 on August 11. By August 12, convective available potential energy (CAPE) reached $>1800 \text{ J kg}^{-1}$
1075 ¹ at sounding sites in the SEUS, leading to scattered Cbs forming in the early morning hours over
1076 Tennessee and southeastern Missouri, and propagating into northern Alabama as the day
1077 progressed. A significant line of convection reached the northwestern corner of Alabama at 18:00
1078 UTC (where it was sampled by the DC-8 at $\sim 19:00$ UTC), and subsequent convection that
1079 formed on the eastward propagating outflow boundary reached the UAH lidar site 6 hours later.

1080 Regional aerosol loadings for August 12 were consistent with air masses staying within the
1081 SEUS over the past several days. AERONET AOD registered a 550 nm AOD of 0.18 at
1082 Huntsville in the morning, and Terra MODIS AODs at 550 nm were reported that morning at
1083 0.27 in the vicinity of the Cb sampled. At the surface, regional PM_{2.5} stations were reporting
1084 daily averaged mass concentrations of 5-10 $\mu\text{g m}^{-3}$ at CSN and SEARCH sites. Specifically at
1085 Huntsville, CSN PM_{2.5} ranged from 10-14 $\mu\text{g m}^{-3}$ at daybreak and morning hours, dropping to 5-
1086 10 $\mu\text{g m}^{-3}$ in the afternoon. Global models (e.g., Session et al., 2015) suggested no significant
1087 long range aerosol transport into the region aside from a pulse of African dust around August 8
1088 and 9, three days before the case day studied here. There was no indication of smoke from the
1089 Western United States impacting the area. HYSPLIT trajectories spawned at Huntsville were
1090 consistent with transport via westerly winds on that day, in an air mass isolated from more
1091 pollution in the north. Two day back trajectories showed that the middle troposphere air never
1092 deviated from northeastern Mississippi and northwestern Alabama. Specific trajectories for Ac
1093 layers identified also show origins from storms within this region over 350 km away (Fig. A.3).
1094 All analyses indicate air masses near the surface through the middle troposphere were regional to
1095 the SEUS over the past two days, representative of more regional pollution embedded in a
1096 regional convective regime.

1097 NEXRAD returns and satellite cloud temperatures (Fig. A.3) and demonstrate the textural
1098 changes in cloud fields as the day progressed from widespread cloudiness to more isolated cells.
1099 Above the mixed layer, the sounding was moist but cloud-free, with minor inversions at 3.4 km
1100 (perhaps indicating the top of the PBL), 4.6 (0°C) and 6.2 km heights. Winds were near constant
1101 at 250° above the mixed layer, and with steady increases to 12 m s⁻¹ at the 0°C melting level at 5
1102 km providing only a modest amount of shear (Fig 3(c)). Based on the satellite imagery and
1103 NEXRAD, the fetch of the air mass over northern Alabama was over mostly Cu to a few isolated
1104 but non-precipitating TCu clouds. The CAPE derived from the UAH sounding was 1650 J kg⁻¹,
1105 slightly lower than all of the operational soundings surrounding the site at 12:00 (including
1106 Birmingham to the south at 1831 J kg⁻¹ and Nashville to the north at 1811 J kg⁻¹). This neutral
1107 state in a convective regime is the midday backdrop against which investigations of clouds in the
1108 vicinity of isolated cells is performed in Section 4. By late afternoon, the region was more
1109 convectively developed, with larger but more scattered individual storms. The one observed by

1110 the DC-8 began developing at 19:00 UTC and was monitored until 20:00 UTC. The location of
1111 the DC-8 is marked on Fig A.2 (e) and (f), although the exact precipitating cell monitored was
1112 not observable by NEXRAD until 19:35 when the cloud top height grew to above 6 km. The last
1113 NEXRAD return for this cell was at 20:00 UTC.

1114 As the day progressed, Cbs repeatedly reformed and then propagated eastward, with one cell in a
1115 mature phase reaching UAH site at 23:00 UTC. This pattern of afternoon thunderstorms
1116 persisted for several more days, when large scale subsidence began to develop behind a weak
1117 front that passed through on August 14.

1118 At most levels at temperatures below -9°C intermittent ice was observed on the SPEC probes
1119 (Fig. A.5). The SPEC cloud particle probes indicate ice was observed beginning about 19:27
1120 UTC, at temperatures near -9°C , ranging in size up to around 400-500 μm . Ice is observed on the
1121 subsequent climb to colder temperatures at 19:34 UTC (-10°C), extending to sizes on the order
1122 of 1 mm. Intermittent ice, like that observed by the 2D-Stereo particle probe and shown in Fig
1123 A.5, is observed at subsequently colder temperatures. The 2D-S (Lawson et al. 2006) is a 2-
1124 dimensional stereo particle optical array probe that records the cross sectional image of particles
1125 from 10 μm to a few mm in size with 10 μm resolution for determining particle size,
1126 concentration, extinction, phase, and ice particle habit.

1127

1128 **10. References**

1129 Ackerman, S. A., Toon, O. B., and Hobbs, P. V.: A model for particle microphysics, turbulent
1130 mixing, and radiative transfer in the stratocumulus-topped marine boundary layer and
1131 comparisons with measurements, *J. Atmos. Sci.*, 1204-1236, doi:10.1174/1520-
1132 0469(1995)052<1204;AMFPMT>2.0.CO; 1995.

1157 Alfaro-Contreras, R., Zhang, J., Reid, J. S., and S. Christopher S.: A study of 15-year aerosol
1158 optical thickness and direct shortwave aerosol radiative effect trends using MODIS, MISR,
1159 CALIOP and CERES, *Atmos. Chem. Phys.*, 17, 13849-13868, [https://doi.org/10.5194/acp-](https://doi.org/10.5194/acp-17-13849-2017)
1160 [17-13849-2017](https://doi.org/10.5194/acp-17-13849-2017), 2017.

1161 Barrett, A. I., Hogan, R. J., and Forbes, R. M.: Why are mixed-phase altocumulus clouds poorly
1162 predicted by large-scale models? Part 1. Physical processes, *J. Geophys. Res. Atmos.*
1163 *Atmospheres*, 122, 9903–9926, doi: 10.1002/2016JD026321, 2017.

1164 Campbell, J. R., Vaughan, M. A., O, M., Holz, R. E., Lewis, J. R., and. Welton, E. J:
1165 Distinguishing cirrus cloud presence in autonomous lidar measurements, *Atmos. Meas.*
1166 *Tech.*, 8, 435-449, doi: 10.5194/amt-8-435-2015, 2015.

1167 Canagaratna, M. R., Jayne, J. T., Jimenez, J. L., Allan, J. D., Alfarra, M. R., Zhang, Q.,
1168 Onasch, T. B., Drewnick, F., Coe, H., and Middlebrook, A.: Chemical and microphysical

1169 characterization of ambient aerosols with the Aerodyne Aerosol Mass Spectrometer. *Mass*
1170 *Spectrom. Rev.* **2007**, *26* (2), 185–222, 2007.

1171 Canagaratna, M. R., Jimenez, J. L., Kroll, J. H., Chen, Q., Kessler, S. H., Massoli, P.,
1172 Hildebrandt Ruiz, L., Fortner, E., Williams, L. R., and Wilson, K. R.: Elemental ratio
1173 measurements of organic compounds using aerosol mass spectrometry: characterization,
1174 improved calibration, and implications. *Atmos. Chem. Phys.*, *15*, 253–272, 2015.

1175 Clarke, A. D., Varner, J. L., Eisele, F., Mauldin, R.L., Tanner, D. and Litchy, M.: Particle
1176 production in the remote marine atmosphere: Cloud outflow and subsidence during ACE 1, *J.*
1177 *Geophys. Res.*, *103*(D13), 16397–16409, doi: 10.1029/97JD02987, 1998

1178 Cohn, S. A.: "A New Edition of the International Cloud Atlas". *WMO Bulletin*. Geneva: World
1179 Meteorological Organization. **66** (1): 2–7. ISSN 0042-9767, 2017.

1180 Corr, C. A., Ziemba, L. D., Scheuer, E., Anderson, B. E., Beyersdorf, A. J., Chen, G., Crosbie,
1181 E., Moore, R.H., Shook, M., and Thornhill, K. L.: Observational evidence for the convective
1182 transport of dust over the Central United States, *J. Geophys. Res. Atmos.*, *121*, 1306–1319,
1183 doi:10.1002/2015JD023789, 2016.

1184 DeMott, P. J., Rogers, D. C., and Kreidenweis S. M.: The susceptibility of ice formation in upper
1185 tropospheric clouds to insoluble aerosol components, *J. Geophys. Res.*, *102*(D16), 19575–
1186 19584, doi: 10.1029/97JD01138, 1997.

1187 Dunlea, E. J., DeCarlo, A. P. F., Aiken A. C., Kimmel, J. R., Peltier, R. E., Weber, R.
1188 J., Tomlinson, J., Collins, D. R., Shinozuka, Y., and McNaughton C. S.: Evolution of Asian
1189 aerosols during transpacific transport in INTEX-B. *Atmos. Chem. Phys.*, *9*, 7257–7287,
1190 2009.

1191 Eck, T. F., Holben, B. N., Reid, J. S., Arola, A., Ferrare, R. A., Hostetler, C. A.,
1192 Crumeyrolle, B.S. N., Berkoff, T. A., E. J. Welton, S. Lolli, A. Lyapustin, Y. Wang, J. S.
1193 Schafer, D. M. Giles, B. E. Anderson, B. E., Thornhill, K. L., Minnis, P., Pickering, K.,
1194 Loughner, C. P., Smirnov, A., and Sinyuk, A. :Observations of rapid aerosol optical depth
1195 enhancements in the vicinity of polluted cumulus clouds, *Atmos. Chem. Phys.*, *14*, 11633-
1196 11656, doi:10.5194/acp-14-11633-2014, 2014.

1197 Eloranta, E. W.: High Spectral Resolution Lidar Measurements of Atmospheric Extinction:
1198 Progress and Challenges,” in “Aerospace Conference, 2014 IEEE,” (IEEE, 2014), pp. 1–6,
1199 2014.

1200 Eloranta, E. W.: "High Spectral Resolution Lidar", in Lidar: Range-Resolved Optical Remote
1201 Sensing of the Atmosphere, K. Weitkamp editor, Springer-Verlag, New York, 2005.

1202 Falk, M. J., and Larson, V. E., What causes partial cloudiness to form in multilayered midlevel
1203 clouds? A simulated case study, *J. Geophys. Res.*, *112*, D12206, doi:10.1029/2006JD007666,
1204 2007

1205 Fromm, M. O. Torres, O., Diner, D., Lindsey, D., Vant Hull, B., Servranck, R., Shettle, E. P.,
1206 and Li, Z.: Stratospheric impact of the Chisholm pyrocumulonimbus eruption: 1. Earth-
1207 viewing satellite perspective, *J. Geophys. Res.*, *113*, D08202, doi:10.1029/2007JD009153,
1208 2008.

1209 Garay, M. J., de Szoeki, S. P., and Moroney, C. M.: Comparison of marine stratocumulus cloud
1210 top heights in the southeastern Pacific retrieved from satellites with coincident ship-based
1211 observations, *J. Geophys. Res.*, *113*, D18204, doi:10.1029/2008JD009975, 2008.

1212 Guibert, S., Snider, J. R., and Brenguier, J.-L., Aerosol activation in marine stratocumulus
1213 clouds: 1. Measurement validation for a closure study, *J. Geophys. Res.*, 108, 8628,
1214 doi:[10.1029/2002JD002678](https://doi.org/10.1029/2002JD002678), D15, 2003.

1215 Hair, J. W., Hostetler, C. A., Cook, A. L., Harper, D. B., Ferrare, R. A., Mack, T. L., Welch,
1216 W., , L. R., and Hovis F. E., Airborne high spectral resolution lidar for profiling aerosol
1217 optical properties, *Appl. Opt.*, 47, 6734-6752, doi: 10.1364/AO.47.006734, 2008.

1218 Heymsfield, A. J., Miloshevich, L. M., Slingo, A., Sassen, K., and Starr, D. O’C, An
1219 observational and theoretical study of highly super-cooled altocumulus, *J. of the Atmos. Sci.*,
1220 7, 923-945, doi:[10.1175/1520-0469\(1991\)048](https://doi.org/10.1175/1520-0469(1991)048), 1991.

1221 Heymsfield, A. J.: Microphysical structure of stratiform and cirrus clouds, In *Aerosol-Cloud-*
1222 *Climate Interaction*, ed P. V. Hobbs., Academic Press, San Diego, 97-119, 1993.

1223 Hogan, R. J., Francis, P. N., Flentje, H., Illingworth, A. J., Quante, M. and Pelon, J:
1224 Characteristics of mixed-phase clouds. I: Lidar, radar and aircraft observations from
1225 CLARE'98. *Q.J.R. Meteorol. Soc.*, 129: 2089–2116. doi: 10.1256/rj.01.208, 2003.

1226 Holben, B.N., Eck, T. F., Slutsker, I., Tanre, D., Buis, J. P., Setzer, E. Vermote, E., Reagan, J.
1227 A., Kaufman, Y. J., Nakajima, T., Lavenu, F., Jankowiak, I., and Smirnov, A.: AERONET-
1228 a federated instrument network and data archive for aerosol characterization, *Remote Sens.*
1229 *Environ.*, 66, 1-16, doi: 10.1016/S0034-4257(98)00031-5, 1998.

1230 Houze, R. A. (1993), *Cloud Dynamics*, Academic Press Inc., San Diego CA

1231 Jensen, E. J. and Toon, O. B.: (), The potential effects of volcanic aerosols on cirrus cloud
1232 microphysics, *Geophys. Res. Let.*, 19, 1759-1762, doi: 10.1029/92GL01936 1992.

1233 Johnson, R. H., Ciesielski, P. E., and Hart, K. A.: Tropical inversions near the 0C level, *J. Atmos.*
1234 *Sci.*, 53, 1838–1855, 1996.

1235 Johnson, R. H., Rickenbach, T. M., Rutledge, S. A., Ciesiekski, P. E., and Schubert W. H.,
1236 Trimodal characteristics of tropical convection, *J. Clim.*, 12, 2397– 2418, 1999.

1237 Kaufman, Y. J. and Fraser R. S.: The effect of smoke particles on clouds and climate forcing,
1238 *Science*, 277, 1636-1639, 1997.

1239 Kazil, J., Wang, H., Feingold, G., Clarke, A. D., Snider, J. R., and Bandy, A. R.: Modeling
1240 chemical and aerosol processes in the transition from closed to open cells during VOCALS-
1241 REx, *Atmos. Chem. Phys.*, 11, 7491-7514, <https://doi.org/10.5194/acp-11-7491-2011>, 2011.

1242 Kim, S., Huey, L. G., Stickel, R. E., Tanner, D. J., Crawford, J. H., Olson, J. R., Chen, G.,
1243 Brune, W. H., Ren, X., Leshner, R., Wooldridge, P. J., Bertram, T. H., Perring, A., Cohen,
1244 R.C., Lefer, B. L., Shetter, R.E., Avery, M., Diskin, G., and Sokolik, I.: Measurement of
1245 HO₂NO₂ in the free troposphere during the intercontinental chemical transport experiment -
1246 North America 2004, *J. Geophys. Res.-Atmos.*, 112(D12), 2007.

1247 Kulmala, M., Vehkamäki, H., Petäjä, T., Dal Maso, M., Lauri, A., Kerminen, V. M., Birmili,
1248 W., McMurry P. H., Formation and growth rates of ultrafine atmospheric particles: a review
1249 of observations, *J. Aerosol Sci.*, 35, 143-176, doi: 10.1016/j.jaerosci.2003.10.003, 2004.

1250 Lawson, R. P.: Effects of ice particles shattering on the 2D-S probe. *Atmos. Meas. Tech.*, 4,
1251 1361–1381, doi:[10.5194/ amt-4-1361-2011](https://doi.org/10.5194/amt-4-1361-2011), 2011.

1252 Lawson, R. P., Baker, B. A., Schmitt, C. G., and Jensen T. L.: An overview of microphysical
1253 properties of Arctic clouds observed in May and July during FIRE ACE. *J. Geophys. Res.*,
1254 106, 14 989–15 014, doi:[10.1029/2000JD900789](https://doi.org/10.1029/2000JD900789), 2001.

1255 Lawson, R. P., Jensen, E., Mitchell, D. L., Baker, B., Mo, Q., and Pilon, B.: Microphysical
1256 and radiative properties of tropical clouds investigated in TC4 and NAMMA. *J. Geophys.*
1257 *Res.*, 115, D00J08, doi:[10.1029/2009JD013017](https://doi.org/10.1029/2009JD013017), 2010.

1258 Lawson, R. P., O'Connor, D., Zmarzly, P., Weaver, K., Baker, B. A., Mo, Q. and Jonsson H.,
1259 The 2D-S (stereo) probe: Design and preliminary tests of a new airborne, high speed,
1260 highresolution particle imaging probe. *J. Atmos. Oceanic Technol.*, 23, 1462–1477,
1261 doi:[10.1175/JTECH1927.1](https://doi.org/10.1175/JTECH1927.1), 2006.

1262 Larson, V. E., Fleishauer, R. P., Kankiewicz, J. A., Reinke, D. L., and Vonder Haar, T. H.: The
1263 death of an altocumulus cloud, *Geophys. Res. Lett.*, 28, 2609-2612, doi:
1264 [10.1029/2001GL013031](https://doi.org/10.1029/2001GL013031), 2001.

1265 Larson, V. E., Smith, A. J., Falk, M. J., Kotenberg, K. E., and J.-C. Golaz J.-C., What determines
1266 altocumulus dissipation time?, *J. Geophys. Res.*, 111, D19207, doi:[10.1029/2005JD007002](https://doi.org/10.1029/2005JD007002),
1267 2006.

1268 Livingston, J. M., Schmidt, B., Russell, P. B., Podolske, J. R., Redemann, J., and Diskin, G. S.:
1269 Comparison of water vapor measurements by airborne sun photometer and diode laser
1270 hygrometer on the NASA DC-8, *J. Atmos. Ocean. Tech.*, 25, doi:
1271 [10.1175/2008JTECHA1047](https://doi.org/10.1175/2008JTECHA1047), 2008.

1272 Loughner, C. P., Allen, D. J., Pickering, K. E., Zhang, D.-L. Shou, Y.-X., and Dickerson, R. R.:
1273 Impact of fair-weather cumulus clouds and the Chesapeake Bay breeze on pollutant transport
1274 and transformation, *Atmos. Environ.*, 45, 4060–4072, doi:[10.1016/j.atmosenv.2011.04.003](https://doi.org/10.1016/j.atmosenv.2011.04.003).
1275 2011.

1276 Marchand, R., Ackerman, T., Smyth, M. and Rossow W. B.: A review of cloud top height and
1277 optical depth histograms from MISR, ISCCP, and MODIS, *J. Geophys. Res.*, 115, D16206,
1278 doi:[10.1029/2009JD013422](https://doi.org/10.1029/2009JD013422), 2010.

1279 Martin, G.M., Johnson, D. W., and Spice A., The measurement and parametrization of effective
1280 radius of droplets in warm stratocumulus clouds, *J. Atmos. Sci.*, 51, 2823-1842, doi:
1281 [10.1175/1520-1469\(1994\)051<1823:TMAPOE>2.0.CO;2](https://doi.org/10.1175/1520-1469(1994)051<1823:TMAPOE>2.0.CO;2), 1994.

1282 McMillan, W. W., Evans, K. D., Barnet, C. D., Maddy, E. S., Sachse, G. W., and Diskin G. S.:
1283 Validating the AIRS Version 5 CO retrieval with DACOM in situ measurements during
1284 INTEX-A and –B, *IEEE Trans. On Geosciences and Remote Sensing*, 49, 2802-2813). Doi:
1285 [10.1109/TGRS.2011.2106505](https://doi.org/10.1109/TGRS.2011.2106505), 2011.

1286 Minnis, P., Nguyen, L., Palikonda, R., Heck, P. W., Spangenberg, D. A., Doelling, D. R.,
1287 Ayers, J. K., W. L. Smith, Jr., W. L., Khaiyer, M. M, Trepte, C., Avey, L. A., F.-L. Chang, F.-
1288 L., Yost, C. R., Chee, T. L., and Sun-Mack, S.: Near-real time cloud retrievals from
1289 operational and research meteorological satellites. *Proc. SPIE Remote Sens. Clouds Atmos.*
1290 *XIII*, Cardiff, Wales, UK, 15-18 September, 7107-2, 8 pp., ISBN: 9780819473387, 2008.

1291 Moser, D. H. and Lasher-Trapp S.: The Influence of Successive Thermals on entrainment and
1292 dilution in a simulated cumulus congestus, *J. Atmos. Sci.*, 74, 375–392, doi: [10.1175/JAS-D-](https://doi.org/10.1175/JAS-D-16-0144.1)
1293 [16-0144.1](https://doi.org/10.1175/JAS-D-16-0144.1), 2017

1294 Norris, J. R.: On trends and possible artifacts in global ocean cloud cover between 1952 and
1295 1995, *J. Clim.*, 12, 1864-1870, doi: 10.1175/1520-0442(1999)012<1864:OTAPAI>2.0.CO;2,
1296 1999.

1297 Perry, K. D. and Hobbs, P. V.: Further evidence for particle nucleation in clear air adjacent to
1298 marine cumulus clouds, *J. Geophys. Res.*, 99, D11, 22803–22818, doi: 10.1029/94JD01926,
1299 1994.

1300 Platnick, S. and Twomey S., Determining the susceptibility of cloud albedo to changes in droplet
1301 concentration with the Advanced Very High Resolution Radiometer, *J. Appl. Meteor.*, 33,
1302 334-347, doi: 10.1175/1520-0450(1994)033<0334:DTSOCA>2.0.CO;2, 1994.

1303 Podolske, J. R., Sachse, G. W., and Diskin G.S.: Calibration and data retrieval algorithms for the
1304 NASA Langley/Ames Diode Laser Hygrometer for the NASA Transport and Chemical
1305 Evolution Over the Pacific (TRACE-P) mission, *J. Geophys. Res.*, 108, 8792, doi:
1306 10.1029/2002JD003156, 2003.

1307 Posselt, D. J., van den Heever S. C., and Stephens G. L.: Trimodal cloudiness and tropical stable
1308 layers in simulations of radiative convective equilibrium, *Geophys. Res. Lett.*, 35, L08802,
1309 doi: 10.1029/2007GL033029, 2008.

1310 Pruppacher, H. R. and Klett, J. D.: *Microphysics of Clouds and Precipitation*, 2nd Edn., Kluwer,
1311 954 pp., 1997.

1312 Pueschel, R. F., Hallett, J., Strawa, A. W., Howard, S. D., Ferry, G. V., Foster, T., Arnott, W.
1313 P., Aerosol and cloud particles in tropical Anvil: Importance to radiation balanced, *J.*
1314 *Aerosol. Sci.*, 28, 1123-1136, doi: 10.1016/S0021-8502(97)00022-0, 1997.

1315 Parungo, F., Boatman, J. F., Wilkison, S. W., Sievering, H., and Hicks, B. B.: Trends in global
1316 marine cloudiness and anthropogenic sulfur, *J. Climate*, 7, 434–440. doi: 10.1175/1520-
1317 0442(1994)007<0434:TIGMCA>2.0.CO;2, 1994.

1318 Radke, L. F. and P. V. Hobbs (1991), Humidity and particle fields around some small cumulus
1319 clouds, *J. Atmos. Sci.*, 48, 1190–1193, doi:10.1175/1520-0469(1991)0482.0.CO;2. 1992.

1320 Reid, J. S.: Emission, evolution, and radiative properties of particles from biomass burning in
1321 Brazil, dissertation, University of Washington, 1998.

1322 Reid J. S., Hobbs, P. V., Rangno, A. L., and Hegg D. A.: Relationships between cloud droplet
1323 effective radius, liquid water content and droplet concentration for warm clouds in Brazil
1324 embedded in biomass smoke, *J. Geophys. Res.*, 104, 6145-6153, doi: 10.1029/1998JD200119

1325 Reid, J. S., Hyer, E., J., Johnson, R., Holben, B. N., Yokelson, R. J., Zhang, J., Campbell, J.
1326 R., Christopher, S. A., Di Girolamo, L., Giglio, L., Holz, R. E., Kearney, C., Miettinen, J.,
1327 Reid, E. A., Turk, F. J., Wang, J., Xian, P., Zhao, G., Balasubramanian, R., Chew, B. N.,
1328 Janai, S., Lagrosas, N., Lestari, P., Lin, N.-H., Mahmud, M., Nguyen, X. A., Norris, B.,
1329 Oahn, T. K., Oo, M., Salinas, S. V., Welton, E. J., and Liew S. C.: Observing and
1330 understanding the Southeast Asian aerosol system by remote sensing: An initial review and
1331 analysis for the Seven Southeast Asian Studies (7SEAS) program, *Atmos. Res.*, 122, 403-468,
1332 doi: 10.1016/j.atmosres.2012.06.005, 2013.

1333 Reid, J. S., et al. Ground-based High Spectral Resolution Lidar observation of aerosol vertical
1334 distribution in the summertime Southeast United States, *J. Geophys. Res. Atmos.*, 122, 2970–
1335 3004, doi:10.1002/2016JD025798, 2017.

1336 Riihimaki, L. D., McFarlane, S. A., and Comstock J. M., Climatology and formation of tropical
1337 midlevel clouds at the Darwin ARM site, *J. Climate*, 25, 6835–6850, doi:10.1175/JCLI-D-
1338 11-00599.1, 2012.

1339 Riley, E. M., Mapes, B. E., and Tulich, S. N., Clouds associated with the Madden-Julian
1340 Oscillation: A new perspective from CloudSat, *J. of the Atmos. Sci.*, 68, 3032-3051, doi:
1341 10.1175/JAS-D-11-030.1, 2011

1342 Romps, D. M.: A direct measure of entrainment, *J. Atmos. Sci.*, 67, 1908–1927, doi:
1343 10.1175/2010JAS3371.1, 2010.

1344 Romps, D. M., and Kuang Z.: Nature versus nurture in shallow convection, *J. Atmos.*
1345 *Sci.*, 67, 1655–1666, doi: 10.1175/2009JAS3307.1, 2010.

1346 Sachse, G. W., Hill, G. F., Wade, L. O., and Perry M. G.: Fast-response, high precision carbon
1347 monoxide sensor using a tunable diode laser absorption technique, *J. Geophys. Res.*, vol. 92,
1348 no. D2, pp. 2071–2081, 1987.

1349 Saleeby, S. M., S. C. van den Heever, P. J. Marinescu, S. M. Kreidenweis, and P. J.
1350 DeMott: Aerosol effects on the anvil characteristics of mesoscale convective systems, *J.*
1351 *Geophys. Res. Atmos.*, 121, 10,880–10,901, doi: 10.1002/2016JD025082, 2016.

1352 Sassen, K.: The polarization lidar technique for cloud research: a review and current assessment,
1353 *Bull. Am. Meteorol. Soc.*, 72, 1848–1866, 1991.

1354 Sassen, K., Liou, K. N., Kinne, S., and Griffin, M.: Highly supercooled cirrus cloud water:
1355 Confirmation and climate implications, *Science*, 227, 411-413. 1985.

1356 Sassen, K., and Khvorostyanov V. I.: Microphysical and radiative properties of mixed-phase
1357 altocumulus: A model evaluation of glaciation effects, *Atmos. Res.*, **84**, 390–398,
1358 doi:10.1016/j.atmosres.2005.08.017, 2017.

1359 Sassen, K., and Khvorostyanov V. I., Cloud effects from boreal forest fires smoke: evidence for
1360 ice nucleation from polarization lidar data and cloud model simulations, *Environ. Res. Let.*,
1361 3, 025006, doi:10.1088/1748-9326/3/2/025006, 2008.

1362 Sassen, K. and Wang, Z.: The clouds of the middle troposphere: Composition, radiative impact,
1363 and global distribution, *Surv. Geophys.*, 33, 677-691, doi: 10.1007/s10712-011-9163-x, 2012.

1364 Schmidt, J., A. Ansmann, A. J. Bühl, and Wandinger, U.: Strong aerosol–cloud interaction in
1365 altocumulus during updraft periods: lidar observations over central Europe, *Atmos. Chem.*
1366 *Phys.*, 15, 10687-10700, doi:10.5194/acp-15-10687-2015, 2015.

1367 Schmidt, J. M., Flatau, P. J., and Yates R. D.: Convective cells in altocumulus observed with
1368 high-resolution radar, *J. Atmos. Sci.*, 71, 2130-2154, doi: 10.1175/JAS-D-13-0172.1, 2014.

1369 Scott, S. G., Bui, T. P., Chan, K. R., and S. W. Bowen S. W.: The meteorological measurement
1370 system on the NASA ER-2 aircraft, *J. Atmos. Ocean. Tech.*, 7, 525-540, 1990.

1371 Snider, J. R., Guibert, S., Brenguier, J.-L., and Putaud, J.-P. Aerosol activation in marine
1372 stratocumulus clouds: 2. Köhler and parcel theory closure studies, *J. Geophys. Res.*, 108,
1373 8629, doi:[10.1029/2002JD002692](https://doi.org/10.1029/2002JD002692), D15., 2003.

1374 Toon, O. B., et al.: Planning, implementation, and scientific goals of the Studies of Emissions
1375 and Atmospheric Composition, Clouds and Climate Coupling by Regional Surveys
1376 (SEAC⁴RS) field mission, *J. Geophys. Res. Atmos.*, 121, 4967–5009,
1377 doi:[10.1002/2015JD024297](https://doi.org/10.1002/2015JD024297). 2016.

1378 Twomey, S.: The Influence of Pollution on the Shortwave Albedo of Clouds, *J. Atmos. Sci.*, 34,
1379 1149-1152., doi: 10.1175/1520-0469(1977)034<1149:TIOPOT>2.0.CO;2, 2017.

1380 Vay, S. A., Choi, Y., Vadrevu, K. P., Blake, D. R., Tyler, S. C., Wisthaler A., Hecobian, A.,
1381 Kondo, Y., G. S. Diskin, D. S., Sachse, G. W., Woo, J. –H., Weinheimer A. J., . Burkhardt, J.
1382 F., Stohl A., and, P. O. Wennberg, P. O, Patterns of CO₂ and radiocarbon across high
1383 northern latitudes during International Polar Year 2008, *J. Geophys. Res.*, 116, D14301,
1384 doi:10.1029/2011JD015643, 2011.

1385 Waddicor, D. A., Vaughan, G., Choulaton, T. W., Bower, K. N., Coe, H., Gallagher, M.,
1386 Williams, P. I., Flynn, M., Volz-Thomas, A., Pätz, H.-W., Isaac, P., Hacker, J., Arnold, F.,
1387 Schlager, H., and Whiteway J. A.: Aerosol observations and growth rates downwind of the
1388 anvil of a deep tropical thunderstorm, *Atmos. Chem. Phys.*, 12, 6157-6172, doi: 10.5194/acp-
1389 12-6157-2012, 2012.

1390 Wang, W., Sheng, L., Jin., H., and Han, Y.: Dust aerosol effects on cirrus and altocumulus clouds
1391 in Northwest China, *J. Meteor. Res.*, 29, 793-805. doi: 10.1007/s13351-015-4116-9, 2015.

1392 Wang, Z., Sassen, K., Whiteman, D. N., Demoz, B. B.: Studying altocumulus with ice verga
1393 using ground based active and passive remote sensors, *J. Appl. Meteor.*, 43, 449-460, doi:
1394 10.1175/1520-0450(2004)043<0449:SAWIVU>2.0.CO;2, 2004.

1395 Wang, G., Zhang, R., Gomez et al., M. E.: Persistent sulfate formation from London Fog to
1396 Chinese haze, *Proceedings of the National Academy of Sciences*, 113, 13630-13635, doi:
1397 10.1073/pnas.1616540113, 1998.

1398 Warren, S. G.: Global distribution of total cloud cover and cloud type amount over the ocean.
1399 *NCAR Tech. Note TN-317 STR*, 212 pp., 1988.

1400 Warren, S.G., Hahn, C. J., London, J., Chervin, R. M., Jenne, R.: Global distribution of total
1401 cloud cover and cloud type amount over land, *NCAR Tech. Note TN-273 STR*, 229 pp., 1986.

1402 Wonaschuetz, A., Sorooshian, A., Ervens, B., Chuang, P. Y., Feingold, G., Murphy, S. M.,
1403 deGouw, J., Warneke, C., and H. H. Jonsson, H. H.: Aerosol and gas re-distribution by
1404 shallow cumulus clouds: An investigation using airborne measurements, *J. Geophys. Res.*,
1405 117, D17202, doi: 10.1029/2012JD018089, 2012.

1441 Yang, Q., Easter, R. C., Campuzano-Jost, P., Jimenez, J. L., Fast, J. D., Ghan, S. J., Wang, H.,
1442 Berg, L. K., Barth, M. C., Liu, et al. Y., Aerosol transport and wet scavenging in deep
1443 convective clouds: A case study and model evaluation using a multiple passive tracer analysis
1444 approach, *J. Geophys. Res. Atmos.*, 120, 8448–8468, doi:10.1002/2015JD023647, 2015.

1445 Yeo, K. and Romps D. M.: Measurement of convective entrainment using Lagrangian
1446 particles, *J. Atmos. Sci.*, 70, 266–277, doi: 10.1175/JAS-D-12-0144.1, 2013.

1447 Yasunga, K., A. Hashimoto, and Yoshizaki, M.: Numerical simulations of the formation of
1448 melting-layer cloud, *Mo. Wea. Rev.*, 136, 223-241, DOI: 10.1175/2007MWR2012.1. 2008.

1449 Yasunaga, K., Yoneyama, K., Kubota, H., Okamoto, H., Shimizu, A., Kumagai, H., Katsumata,
1450 M., Sugimoto, N., and Matsui I.: Melting layer cloud observed during the R/V Mirai Cruise
1451 MR01-K05. *J. Atmos. Sci.* 63, 3020–3032. <https://doi.org/10.1175/JAS3779.1>, 2006.

1452 Zhang, D., Wang, Z., and Liu D.: A global view of midlevel liquid-layer topped stratiform cloud
1453 distribution and phase partition from CALIPSO and CloudSat measurements, *J. Geophys.*
1454 *Res.*, 115, D00H13, doi: 10.1029/2009JD012143, 2010.

1455 Zhang D., Wang, Z., and Liu, D.: Spatial scales of altocumulus clouds observed with collocated
1456 CALIPSO and CloudSat measurements, *Atmos. Res.*, 149, 58-69, doi:
1457 10.1016/j.atmosres.2014.05.023, 2014.

1458 Ziemba L. D., Thornhill, K. L., Ferrare, R., Barrick, J., Beyersdorf, A. J., Chen, G.,
1459 Crumeyrolle, S. N., Hair, J., Hostetler, C., Hudgins, C., Obland, M., Rogers, R., Scarino,
1460 A. J., Winstead, and E. L., and Anderson, B. E.: Airborne observations of aerosol extinction
1461 by in situ and remote-sensing techniques: Evaluation of particle hygroscopicity, *Geophys.*
1462 *Res. Lett.*, 40, 417–422, doi: 10.1029/2012GL054428, 2013.

1463 Zipser, E. J.: Some views on hot towers after 50 years of tropical field programs and two years
1464 of TRMM data. Cloud Systems, Hurricanes, and the Tropical Rainfall Measuring Mission
1465 (TRMM): A Tribute to Dr. Joanne Simpson, *Meteor. Monogr.*, No. 51, *Amer. Meteor. Soc.*,
1466 50–59, 2003.

1467

1468

1469

1470

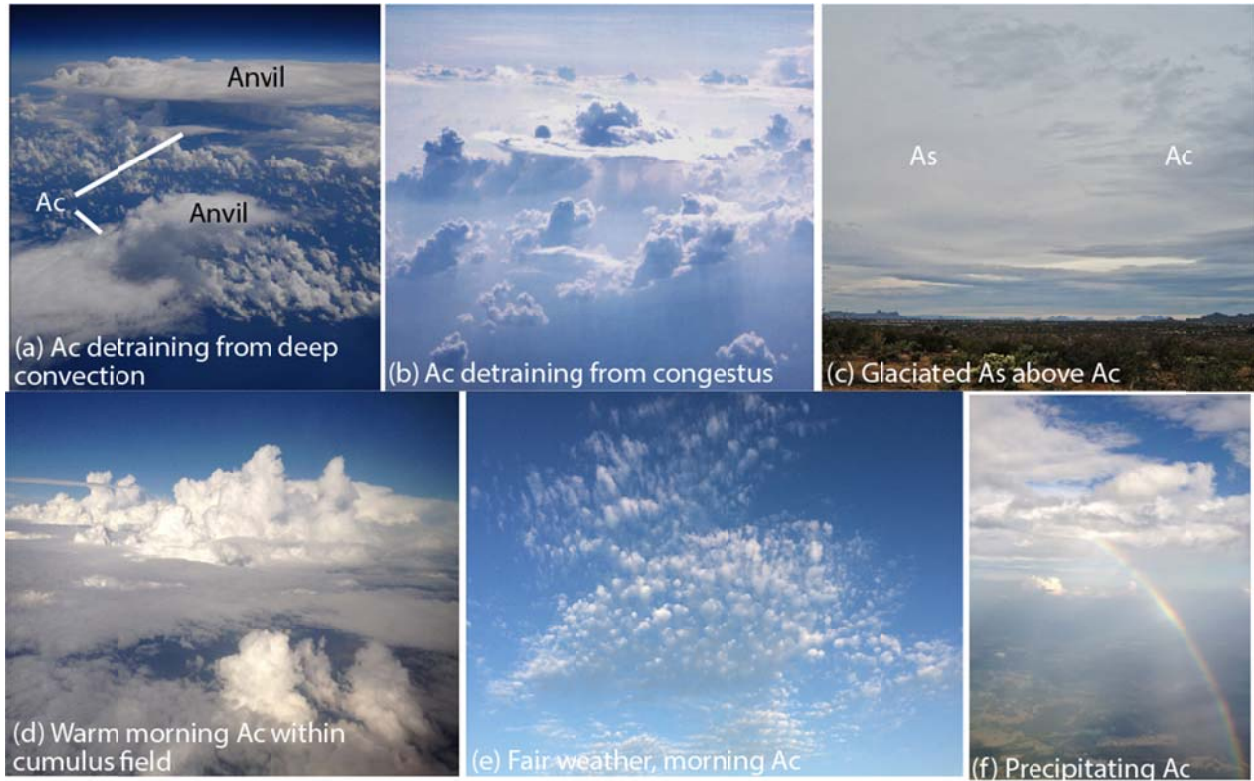
1471

1472

Table 1. Key physical attributes (mean and \pm standard deviation) of detrainment layers observed from the August.12, 2017 thunderstorm. Included are altitude in mean sea level (\sim 300 m higher than above ground level), temperature and water vapor mixing ratio (ω_v), carbon monoxide (CO), Carbon Dioxide (CO₂), Sulfur Dioxide(SO₂) Laser Aerosol Spectrometer (LAS) number and volume at STP, 550 nm dry light scattering for particles less than 1 μ m, and Aerosol Mass Spectrometer (AMS) Organic Carbon (OC) and Sulfate at STP. Layers are defined as shown in Figure 6. [&]Mixed layer properties were taken as a 5 second average just before ascent. *CO instrument was in a calibration cycle for part of this layer. #Upper troposphere

	Altitude (MSL, km)	T (°C)	ω_v (g kg ⁻¹)	CO (ppbv)	CO ₂ (ppmv)	SO ₂ (ppbv)	CN>10 (cm ⁻³)	LAS N (cm ⁻³)	LAS CMD/mode (μ m)	LAS V (μ m ³ cm ⁻³)	LAS VMD/mode (μ m)	σ_s 550 nm (Mm ⁻¹)	f(80)	OC (μ g m ⁻³)	Sulfate (μ g m ⁻³)
ML ^{&}	0.94	22.1	15.5	110	400	200	2300	922	0.13/0.14	2.8	0.22/0.25	18	1.62	4.2	1.5
PBL1	1.55 \pm 0.001	18.1 \pm 0.2	13.3 \pm 0.2	93 \pm 0.6	396 \pm 0.5	339 \pm 483	1600 \pm 70	717 \pm 0.42	0.16/0.16	3.2 \pm 0.3	0.24/0.25	28 \pm 2.5	1.58 \pm 0.02	4.1 \pm 0.3	2.2 \pm 0.4
PBL2	2.9 \pm 0.2	10.5 \pm 1.5	9.4 \pm 0.5	76 \pm 3*	395 \pm 0.5	14 \pm 10	2050 \pm 2300	248 \pm 37	0.14/0.14	1.3 \pm 1.6	0.19/0.20	8 \pm 2	1.60 \pm 0.02	2.2 \pm 0.4	0.6 \pm 0.1
MT1	4.1 \pm 0.1	3.9 \pm 0.6	6.5 \pm 0.4	N/A	393 \pm 0.3	25 \pm 8	1532 \pm 68	112 \pm 20	N/A/ $<$ 0.1	0.31 \pm 0.1	0.20/0.25	3 \pm 2	1.57 \pm 0.04	0.8 \pm 3	0.2 \pm 0.1
MT2	4.6 \pm 0.02	1.0 \pm 0.2	6.2 \pm 0.4	76 \pm 2	396 \pm 0.25	20 \pm 6	1515 \pm 720	125 \pm 36	N/A / $<$ 0.1	0.4 \pm 0.4	0.20/0.20*	3 \pm 2	1.65 \pm 0.02	0.5 \pm 0.2	0.15 \pm 0.1
MT3	6.3 \pm 0.2	-9 \pm 0.1	2.2 \pm 0.8	74 \pm 4	395 \pm 0.25	12 \pm 6	2893 \pm 1013	76 \pm 12	N/A / $<$ 0.1	0.2 \pm 0.5	0.10/0.12	1 \pm 1	N/A	0.2 \pm 0.1	0.1 \pm 0.1
UT1 [#]	7.8 \pm 0.2	-17.3 \pm 0.5	1.8 \pm 0.1	79 \pm 4	395 \pm 0.25	34 \pm 8	N/A	N/A	N/A / $<$ 0.1	N/A	N/A	N/A	N/A	0.2 \pm 0.1	0.1 \pm 0.1
UT2 [#]	8.5 \pm 0.1	-21.6 \pm 0.2	0.9 \pm 0.2	80 \pm 2	395 \pm 0.25	32 \pm 8	8258 \pm 1192	62 \pm 10	N/A / $<$ 0.1	0.1 \pm 0.1	$<$ 0.1/0.12	1 \pm 1	N/A	0.2 \pm 0.1	0.1 \pm 0.1
UT3 [#]	9.7 \pm 0.1	-30.4 \pm 0.3	0.3 \pm 0.1	76 \pm 4	395 \pm 0.25	3 \pm 8	7687 \pm 1980	59 \pm 12	N/A / $<$ 0.1	0.3 \pm 1.3	$<$ 0.1/0.12	1 \pm 1	N/A	1 \pm 0.3	1 \pm 0.3
UT4 [#]	10.5 \pm 0.2	-38 \pm 2.3	0.4 \pm 0.1	78 \pm 1	395 \pm 0.25	23 \pm 20	N/A	N/A	N/A / $<$ 0.1	N/A	N/A	N/A	N/A	0.6 \pm 0.4	0.2 \pm 0.1

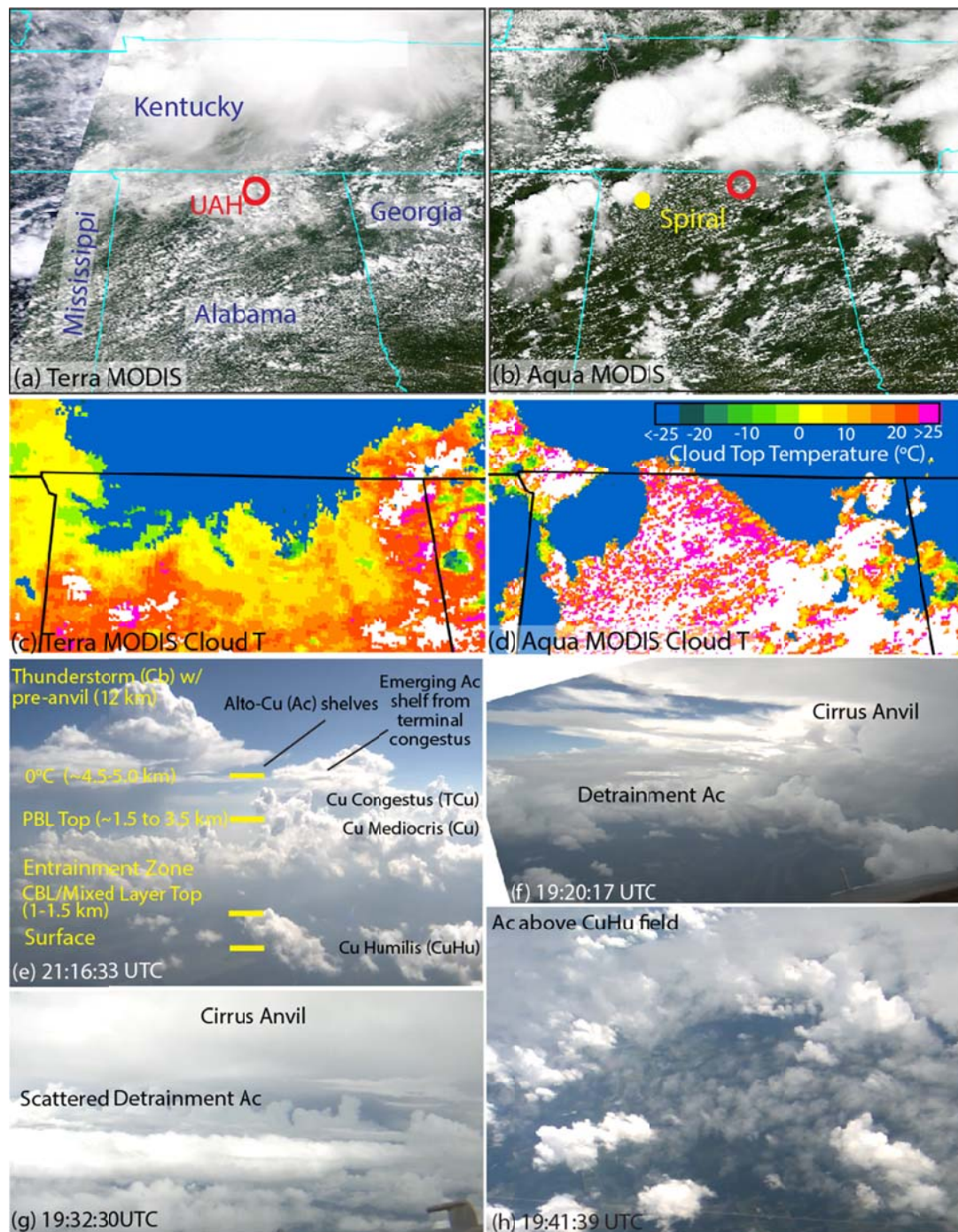
1
9



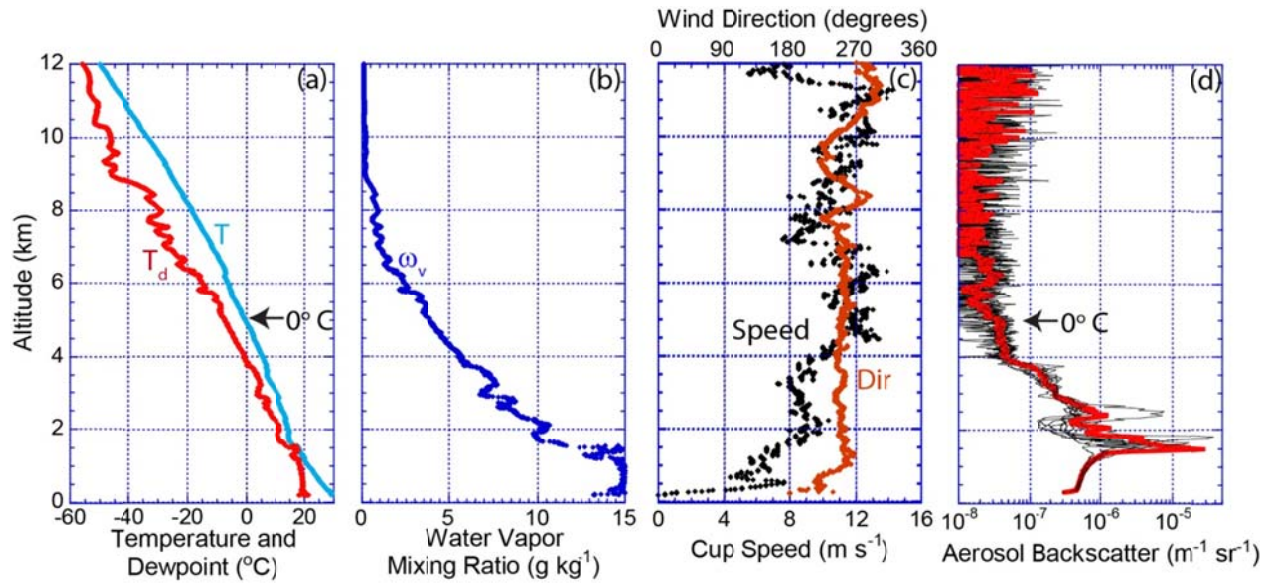
10
11
12

13 Figure 1. Cloud photographs of Ac and As characteristics. (a) Image from the NASA ER-2
14 showing Ac shelf clouds detrain from deep convection over the Gulf of Mexico during
15 SEAC⁴RS; (b) Ac detrain from Cumulus congestus in a field of biomass burning smoke over
16 Brazil (Reid et al., 1999); (c) mixed field of As above Ac clouds during a convectively active
17 period in Arizona ; (d) Warm Ac clouds over developing cumulus field over west Texas during
18 SEAC⁴RS ; (e) Morning fair weather Ac field over Monterey CA; (f) precipitating thin Ac clouds
19 over central Texas during SEAC⁴RS (Photo credit, (a) S. Broce, NASA; (b) & (c) A. Rangno,
20 enhanced for contrast; (d) - (f), J. S. Reid).

21
22
23



24
 25 Figure 2. MODIS (a) Terra (16:00 UTC) and (b) Aqua (19:14 UTC) images, with markers
 26 indicating the location of the UAH lidar site (red) and DC-8 spiral (yellow) for August 12, 2013.
 27 Corresponding MYD06 cloud top temperatures zoomed onto northern Alabama are provided in
 28 (c) and (d). Also included are annotated camera images from the NASA DC-8 demonstrating
 29 cloud types (e) image just after profile components end; (f) forward images as the DC-8 was
 30 about to enter a detrainment Ac at 4.4 km (g) forward image of the DC-8 while sampling 6.5 km
 31 aerosol layer; (h) nadir images of an Ac detrainment shelf exiting a Cb over a field of Cu.



32

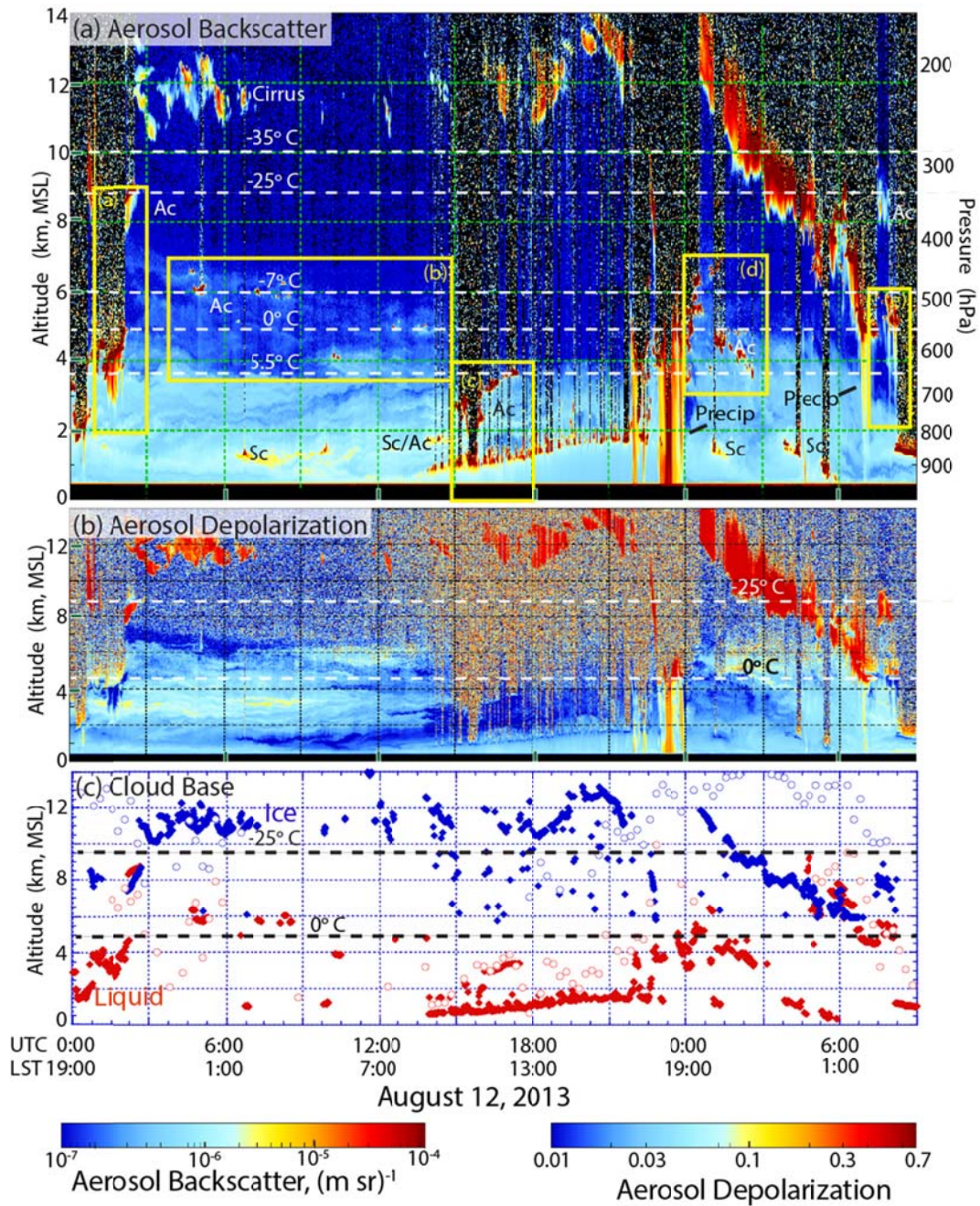
33 Figure 3. SEACIONS radiosonde release on August 12, 2013 18:40 Z/13:40 CDT at Huntsville
 34 (altitude in MSL, 200 m greater than ground level). (a) Temperature and dewpoint; (b) water
 35 vapor mixing ratio; (c) wind cup speed and direction. (d) 5 minute aerosol backscatter profiles
 36 from the UW-HSRL at Huntsville for the two hours after the radiosonde release, with the mean
 37 value in red.

38

39

40

41

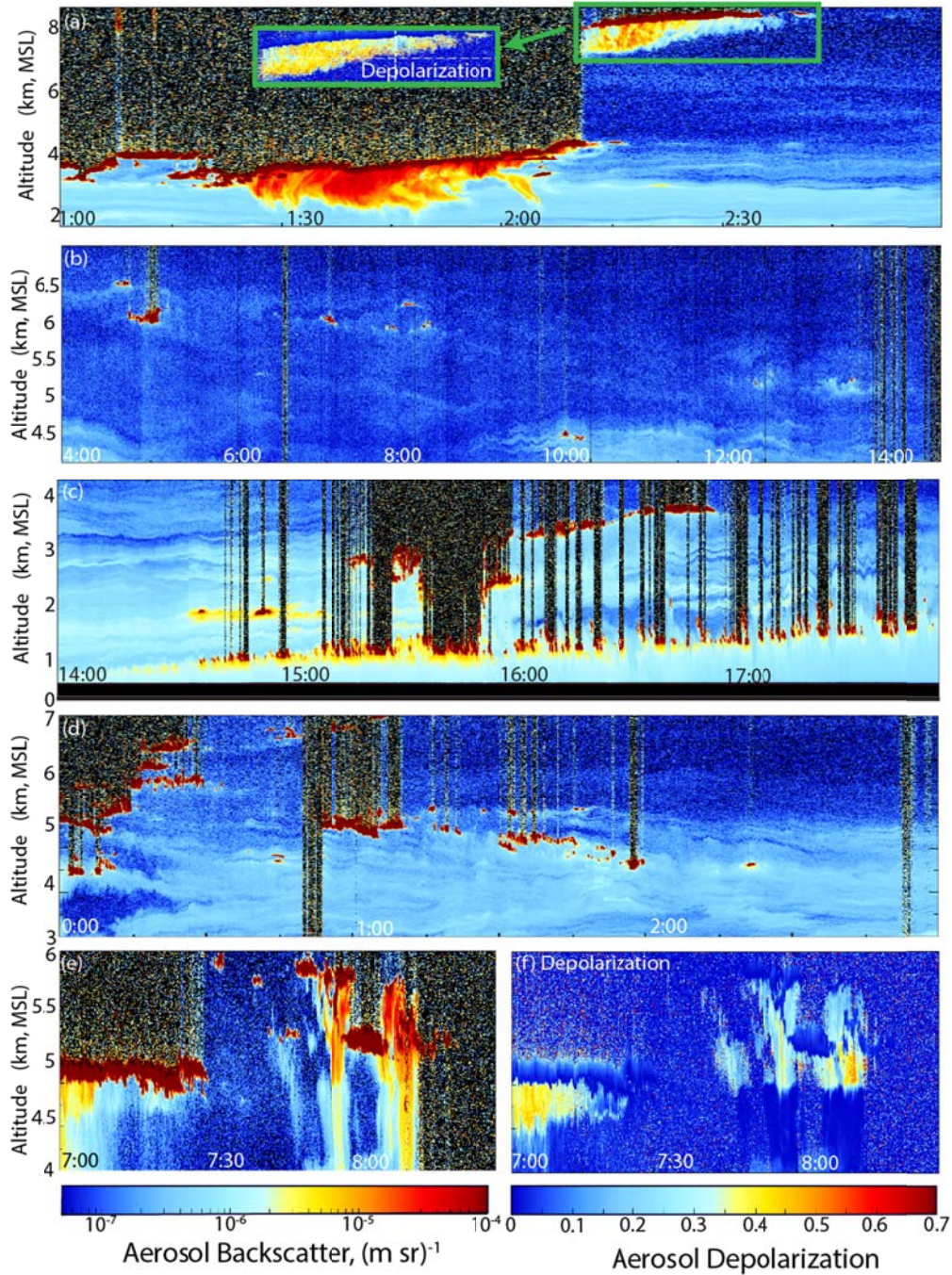


42

43

44 Figure 4. Example lidar data for August 12, 2013. UW HSRL aerosol (a) backscatter and (b)
 45 depolarization from the surface to 14 km AGL. Listed are cloud types, phenomenon and, from a
 46 13:30 radiosonde release, key temperature isopleths. Also shown in (c) are liquid and ice cloud
 47 bases (solid) from the ground based HSRL, and liquid and cloud tops from GOES-13 (open). To
 48 convert from AGL to MSL, subtract 220 m.

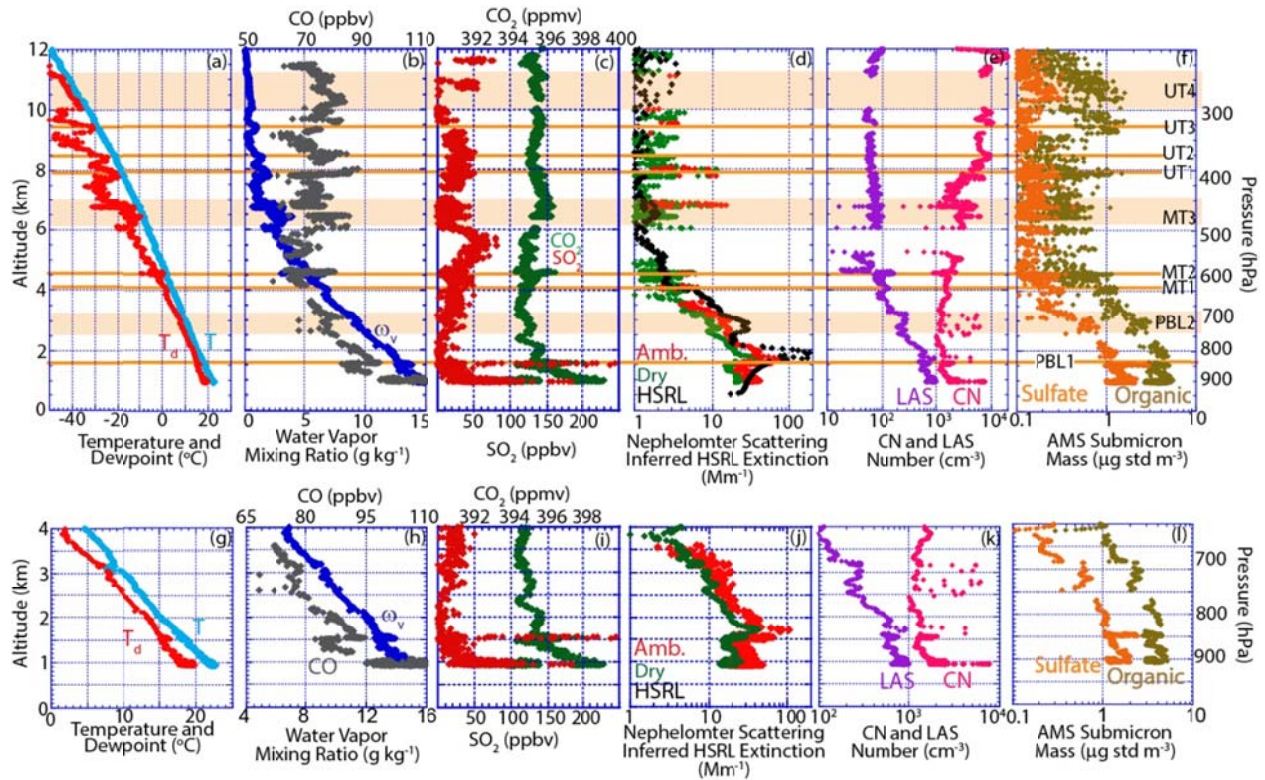
49



51

52 Figure 5. Aerosol backscatter for inset boxes as labeled in Figure 4 of key altocumulus and
 53 aerosol features for the August 12, 2013 case. Included is aerosol depolarization where ice is
 54 prevalent including an inset in (a), and a depolarization in (f) corresponding to (e). All times are
 55 UTC.

56

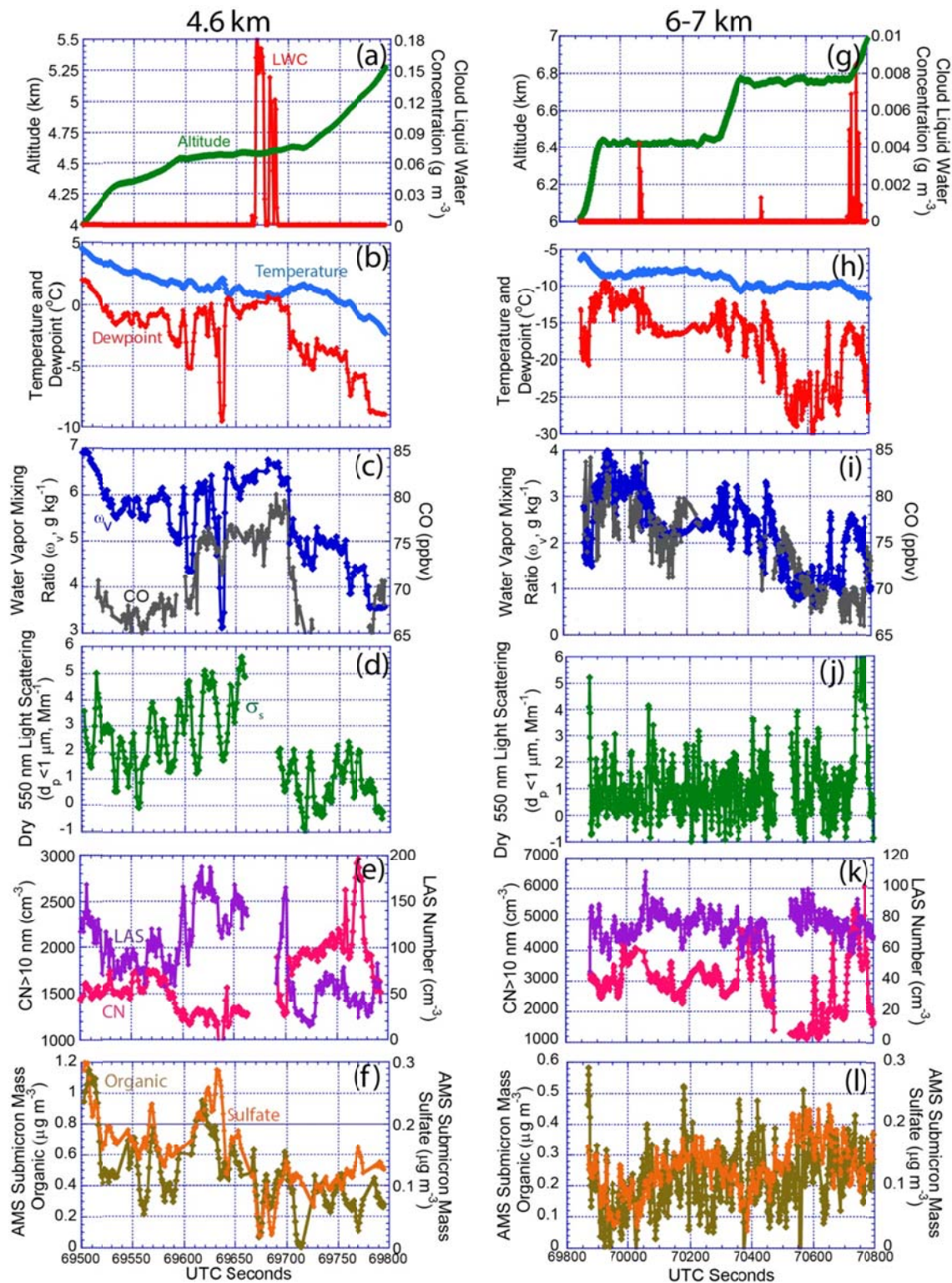


58

59 Figure 6. DC-8 aircraft spiral sounding data initiated at August 12, 2013 19:10:30 UTC on the
 60 downwind side of a thunderstorm over northwest Alabama. Altitudes are relative to mean sea
 61 level, ~ 300 m higher than AGL. Included is (a) Temperature and dew point; (b) Water vapor
 62 mixing ratio (ω_v) and CO; (c) CO₂ and SO₂; (d) DC-8 total ambient and fine dry 550 nm
 63 nephelometer with the ground based UW HSRL derived extinction (lidar ratio= 55 sr^{-1}) at
 64 Huntsville AL; (e) Number concentration from laser aerosol spectrometer (LAS, $d_p > 0.1 \mu\text{m}$) and
 65 condensation nuclei (CN, $d_p > 10 \text{ nm}$); (f) Aerosol mass spectrometer organic materials and
 66 sulfate. Key moisture and aerosol layers as discussed in the text are marked as orange lines or
 67 bands. (g)-(f), same as (a)-(e) expanded in the vertical to enhance PBL feature readability and the
 68 legends are equivalent.

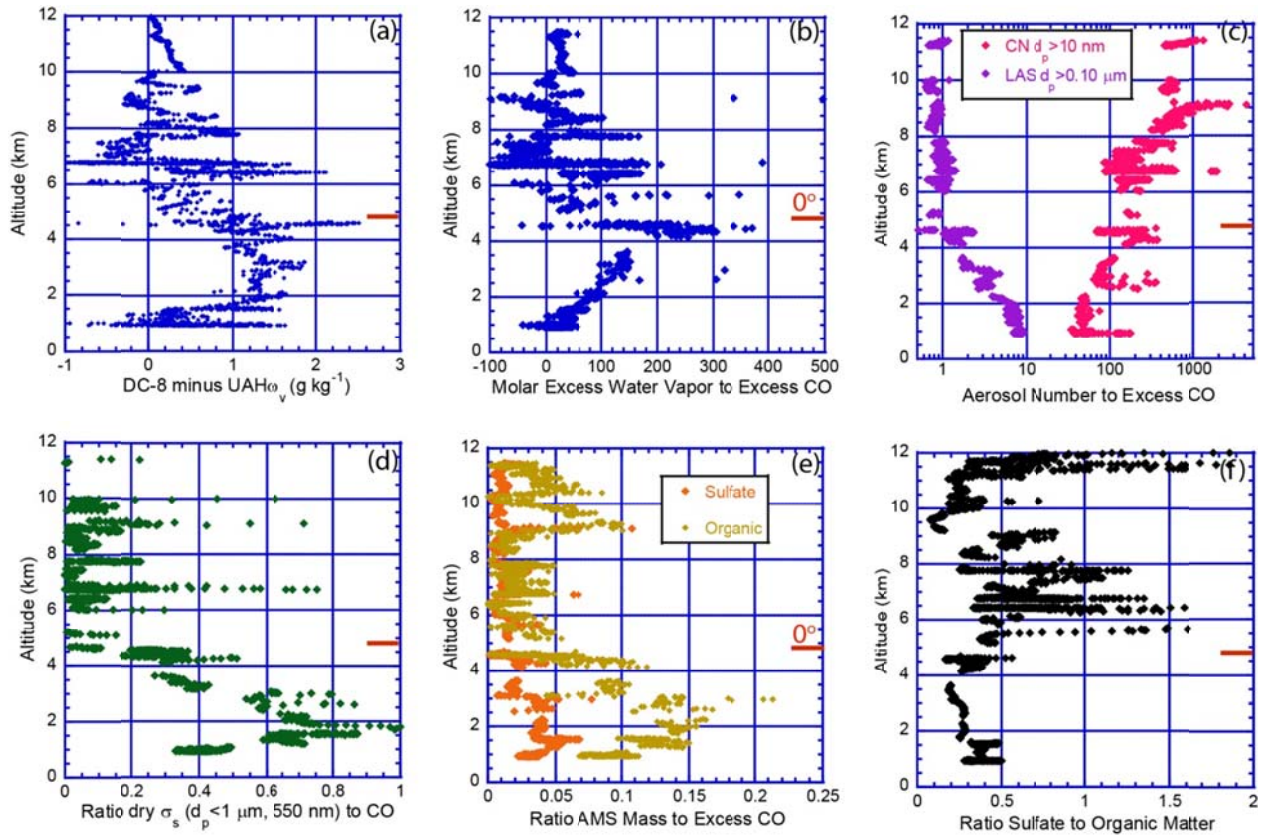
69

70



71
 72 Figure 7. Time series of key meteorology, cloud and aerosol properties entering a detrainment
 73 shelf cloud on Aug 12, 2014. The legends for the graphs on the left are the same for graphs on
 74 the right

75



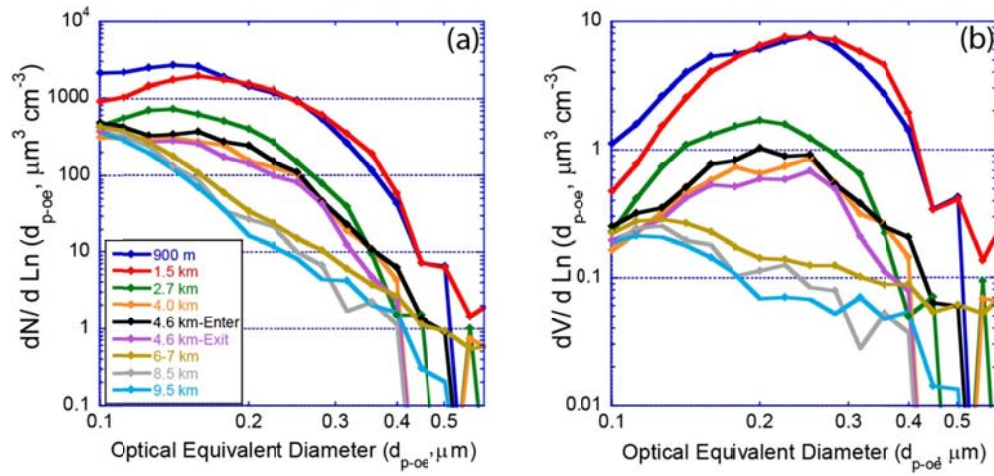
76

77

78 Figure 8. (a) Difference in water vapor mixing ratio between the DC-8 profile and the
79 SEACONS Aug 12, 2013 radiosonde release at Huntsville, AL. Profiles of key constituents
80 relative to excess CO including (b) excess water vapor to excess CO; and (c) aerosol number; (d)
81 dry light scattering; (e) organic carbon and sulfate to excess CO; (f) ratio of sulfate to particulate
82 organic matter.

83

84



85

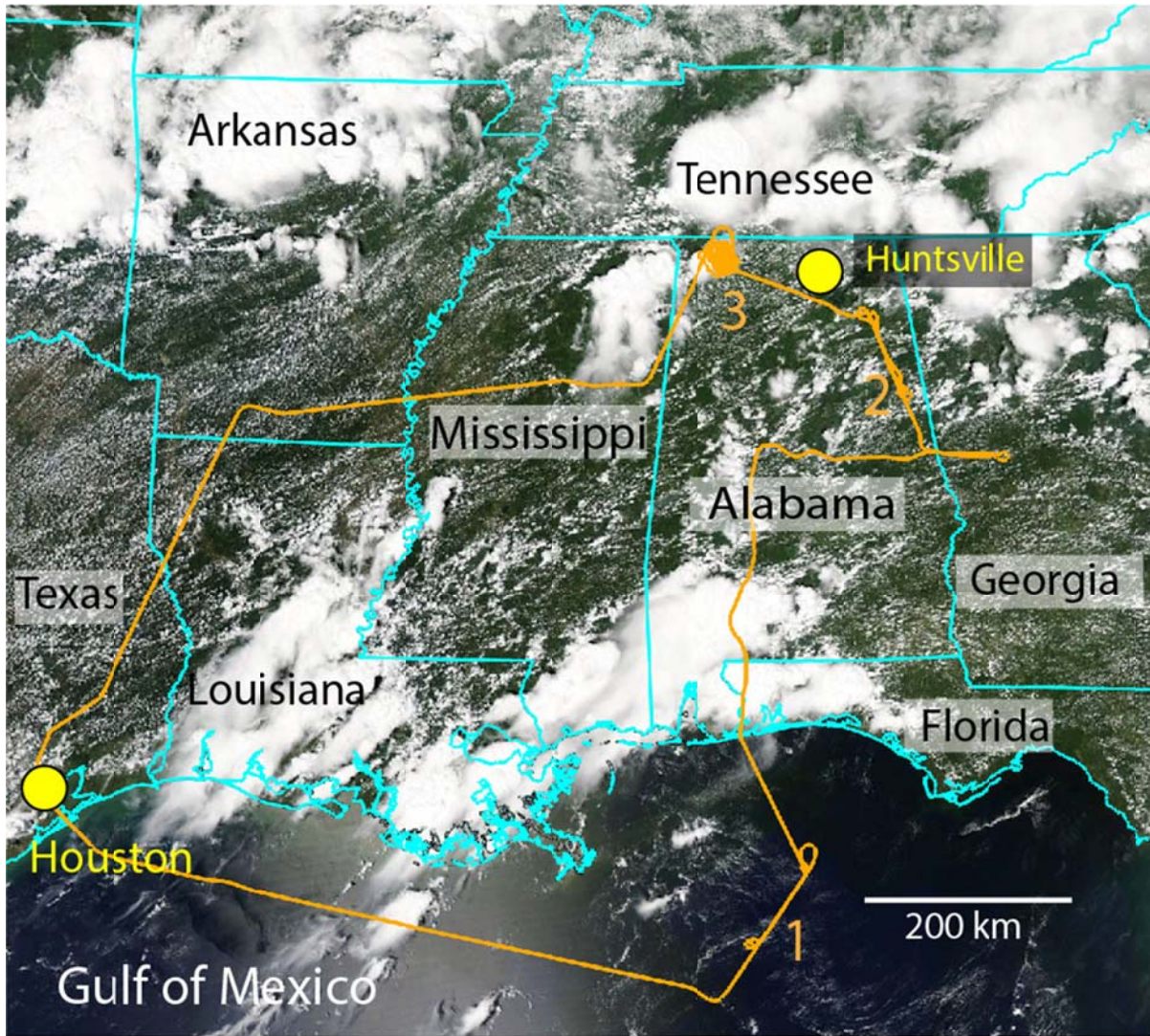
86 Figure 9. Laser Aerosol Spectrometer-LAS (a) number and (b) volume distributions of aerosol
87 layers as a function of altitude. The legends for the two graphs are the same.

88

89

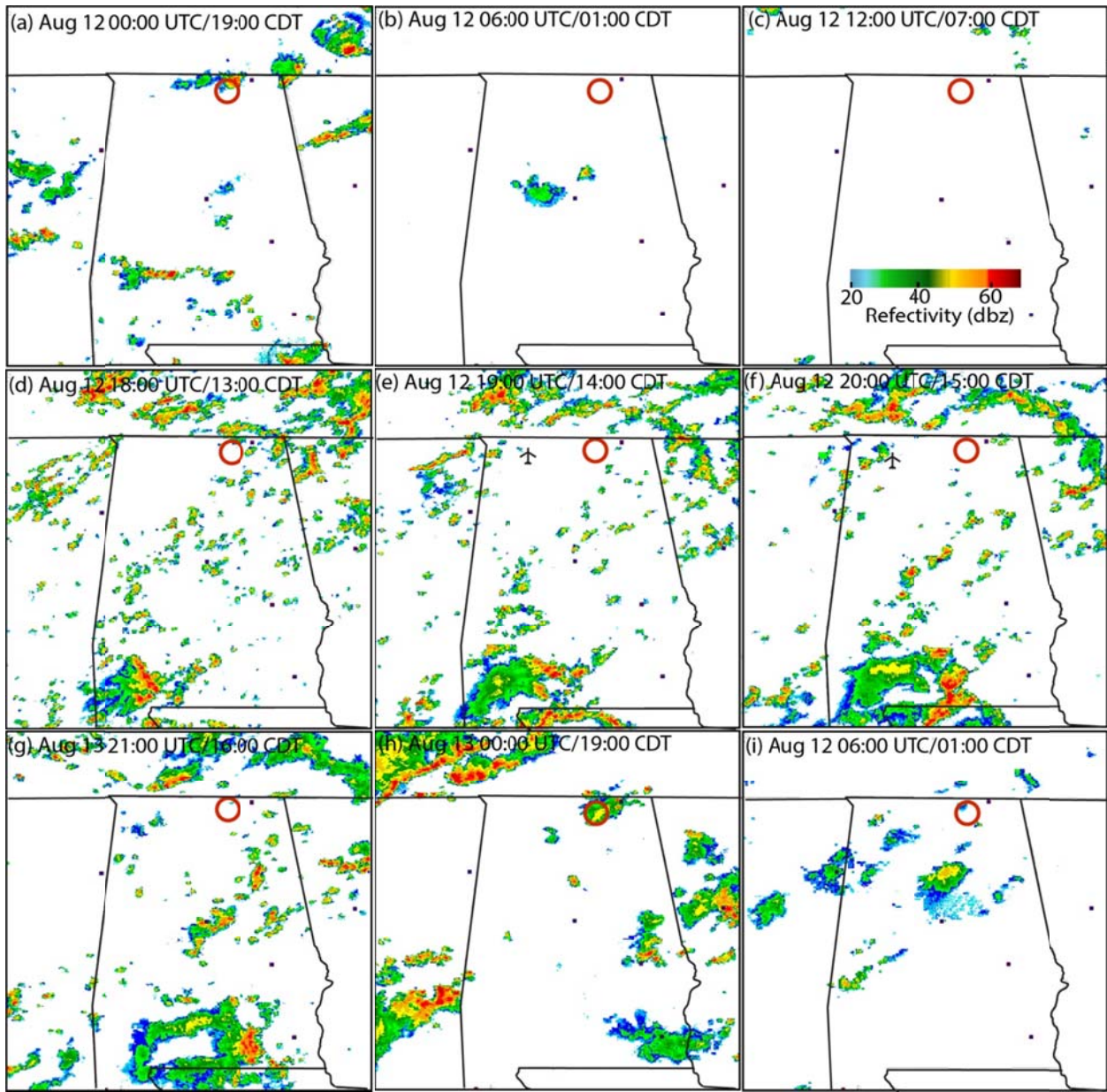
90

91



92

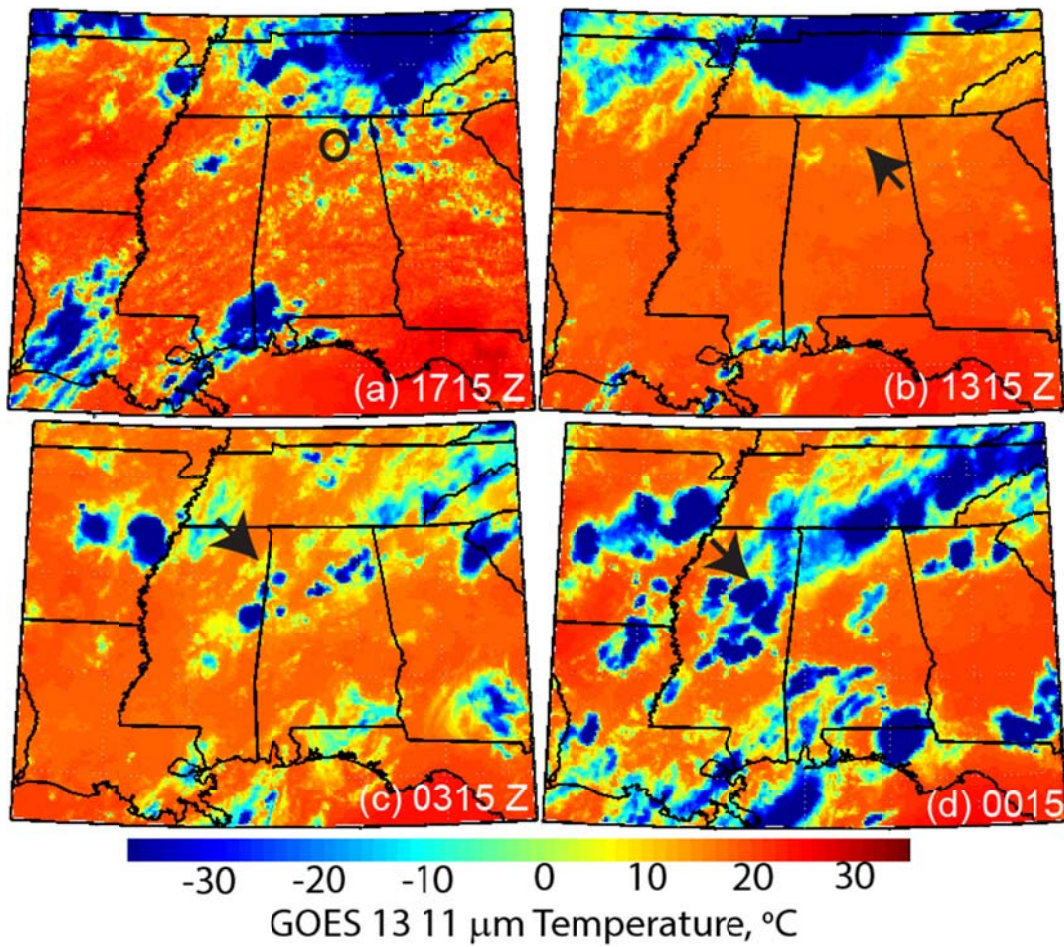
93 A.1 Flight track for the NASA DC-8 (orange) overlaid on the August 12, 2013 Aqua MODIS
 94 RGB image. Takeoff and landing were at Houston, Texas. The HSRL site at Huntsville Alabama
 95 is likewise marked. Coordinated curtain wall profiles with the ER-2 were conducted at labels 1 &
 96 2, followed by the convection spiral discussed at length here at point 3.



97

98 Figure A.2. NEXRAD radar reflectivity composites for August 12, 2013 study case. The red
 99 circle indicates the location of the Huntsville HSRL site and black aircraft the location of the
 100 DC-8 sampling the cell studied here.

101



102

103 Figure A.3. GOES 13 11 μm channel images of the storm leading to AC clouds in the Huntsville
 104 lidar data in Figure 5. (a) 12 Aug 2013, 1715z of PBL detrained AC clouds. (b) Initiation of back
 105 trajectory for 0°C cloud. (c) 10 hrs back trajectory endpoint to large detrainment shelf (d) Cb that
 106 formed the AC layer. What are the arrows for?

107

108

109

110

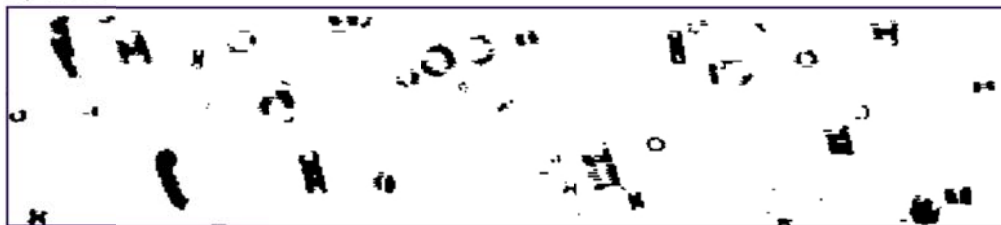
111



112

113 Figure A.4. Forward camera images from the DC-8 forward video taken from the leeward spiral
 114 along the sampled thunderstorm on August 12, 2014 over northwestern Alabama.

a) 19:34:22-24/70440



b) 19:34:24-27/70464



c) 19:34:34-19:38:36/70474



d) 19:38:36-37/70716



e) 19:38:37-38/70717



115

116 Figure A.5. 2D-S images of ice for selected periods during layer sampling associated with the
117 right column of Fig. 7. Temperatures were $\sim -10^{\circ}\text{C}$, at an altitude of 6.75 km. Annulus are ice
118 imaged out of focus.